Harald Matthias Fitzek, BSc

Optimizing the Environmental Scanning Electron Microscope for chamber pressures up to 2700 Pa

MASTER THESIS

For obtaining the academic degree
Diplom-Ingenieur

Master Program of
Technical Physics

Graz University of Technology

Supervisor:
Ao.Univ.-Prof. Dipl.-Ing. Dr.techn. Ferdinand Hofer
Institute of Electron Microscopy and Nanoanalysis and
Graz Centre for Electron Microscopy

Graz, June 6, 2014

Acknowledgment

EIDESSTATTLICHE ERKLÄRUNG

AFFIDAVIT

Ich erkläre an Eides statt, dass ich die vorliegende Arbeit selbstständig verfasst, andere als die angegebenen Quellen/Hilfsmittel nicht benutzt, und die den benutzten Quellen wörtlich und inhaltlich entnommenen Stellen als solche kenntlich gemacht habe. Das in TUGRAZonline hochgeladene Textdokument ist mit der vorliegenden Masterarbeit identisch.

I declare that I have authored this thesis independently, that I have not used other than the declared sources/resources, and that I have explicitly indicated all material which has been quoted either literally or by content from the sources used. The text document uploaded to TUGRAZonline is identical to the present master's thesis.

Datum / Date	Unterschrift / Signature

Contents

1 Abstract

At high pressures the applications of the environmental scanning electron microscope are limited by poor image quality. In this work two modifications are made to the commercial environmental scanning electron microscopes FEI Quanta 600 (field emission gun) and FEI Quanta 200 (thermionic gun). Both modifications significantly improve the image quality at pressures above 500 Pa. The optimizations of the differential pumping system proposed by Monte Carlo simulations are taken into account to design a more versatile bullet (aperture holder). The beam transfer characteristics of the new bullet are studied and it is shown that the new bullet significantly reduces beam losses before the sample chamber. With increasing chamber pressure the amplification of the secondary electron signal decreases. An improved design of a new secondary electron detector is presented and the increase in image quality measured. A computer algorithm is developed that can determine the signal to noise ratio and maximum contrast of a SEM image of a standardized sample. The algorithm is used to test several detector designs and positions and an ideal shape and position for imaging above 500 Pa is determined. The ideal setup is investigated in more detail and the effect of beam scattering on the image quality of the new design is quantified. The limits of the new detector and bullet are estimated suggesting that imaging well beyond 10 kPa should be possible.

2   Introduction

In an environmental scanning electron microscope the gun has to be shielded from the high pressures in the sample chamber by a differential pumping system. This system is realized by a set of pressure limiting apertures (PLA) between the sample chamber, the pump and the column. The pressure from the sample chamber has to be reduced as efficient as possible by the pressure limiting system in order to keep scattering of the beam before the sample chamber to a minimum. Previous studies [1,2,3,4] suggest that the pressure limiting systems currently used in commercial ESEMs are far from ideal. The design flaws pointed out in those papers are taken into account in our design of a new bullet (aperture holder). PLAs with a wide range of diameters can be used with the new bullet. The field of view, the pressure limiting ability and the beam transfer characteristics are investigated. The field of view and the pressure limiting ability of the setup can easily be measured. The beam transfer characteristics are measured using an adaptation of the method proposed by J. Rattenberger[5], which is taking into account the analysis of beam current measurement techniques provided by G.D. Danilatos[6].

In an ESEM the gas in the sample chamber is used to amplify the secondary electron signal. Theoretical models of the gaseous amplification of the secondary electrons(SE)[7] suggest that the amplification is reduced by high pressures in the sample chamber. Therefore SE-detectors have to be adapted in order to function efficiently at high pressures. A measurement technique using a standardized sample and a computer algorithm to determine the signal to noise ratio and maximum contrast of a SEM image of that sample is developed for testing of SE-detector designs. Using a prototype detector the effect of changing the shape and position of the detector on image quality is measured. Based on the results a new setup for pressures above 500 Pa is proposed and the effects of scattering and the chamber pressure on image quality using that setup are investigated in detail. The detailed measurements provide the framework for more efficient detector designs and the means to test them.

3 Fundamentals

3.1 Environmental scanning electron microscope

The key difference between a conventional scanning electron microscope (SEM) and an environmental scanning electron microscope (ESEM) is that in an ESEM, the pressure in the sample chamber can be as high as a couple of kPa, where as a SEM needs a high vacuum in the sample chamber. This has many advantages, since a lot of the limitation for the sample in a SEM can be eliminated. Namely that the sample has to be conductive, vacuum tolerant and that it cannot be wet, which is a major drawback when looking at organic probes. However, the ESEM has some drawbacks as well, namely that the image quality declines with increasing pressure due to scattering, an issue that is being addressed in this work. Also, since there still has to be a high vacuum in the column and gun chamber, a complicated multistage pumping system is necessary in an ESEM. Figure 1 shows a schematic drawing of the pumping system.
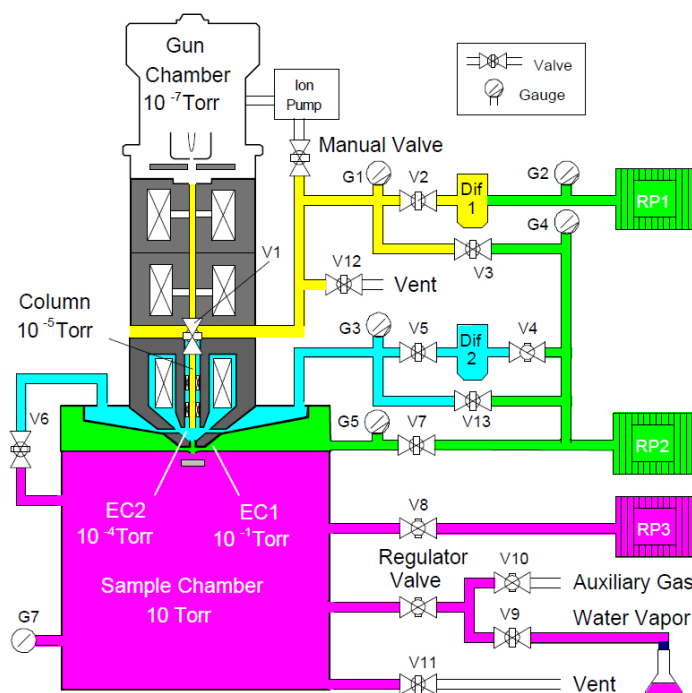

Figure 1: Five stage pumping system in an ESEM [8].

The most important part of the pumping system are the three regions at the bottom of the pole piece, which are the sample chamber(purple), EC1(green) and EC2(blue). In this part of the pumping system a pressure transition of several orders of magnitude is achieve by 2 pressure limiting apertures (PLA) within a couple of mm. Those PLAs are located inside an aperture holder ('bullet'), which is a removable part at the bottom of the pole piece. Figure 2 shows an enlarged schematic drawing of this part.
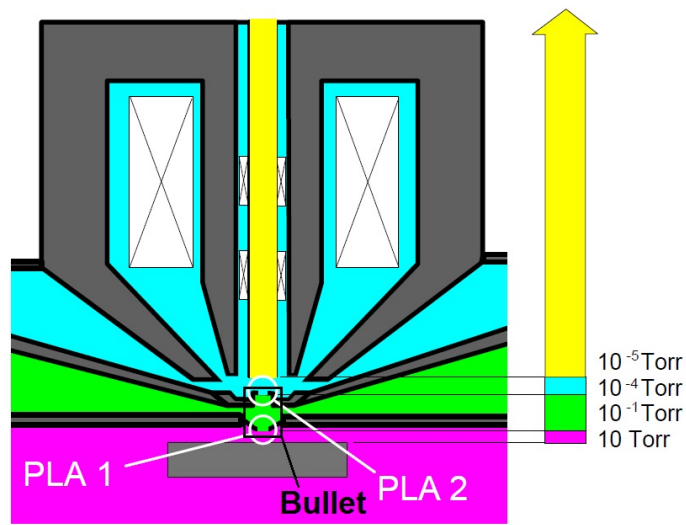
Figure 2: Enlarged schematic drawing of the part of the pumping system at the bottom of the pole piece [8].

Scattering of the electron beam is the main problem of an ESEM, as described in more detail in chapter 3.2. Due to the rapid decline in pressure between the sample chamber and EC2 (blue), virtually all of the scattering takes place in the sample chamber and EC1 (green). The pressure in the sample chamber is given by the experimental requirements, whereas the pressure gradient in EC 1 depends on the size of the PLA 1 and the design of the bullet. Therefore these parts are vital to the quality of an ESEM.

3.2 Electron beam transfer

As mentioned in chapter 3.1 the main issue in an ESEM is the scattering of the electron beam in the imaging gas. However, it does not influence the resolution of the microscope. This is because electrons which are scattered out of the beam, are scattered onto a larger area of the sample compared to those who are not scattered at all and therefore these electrons are merely generating a background, as shown in figure 3.
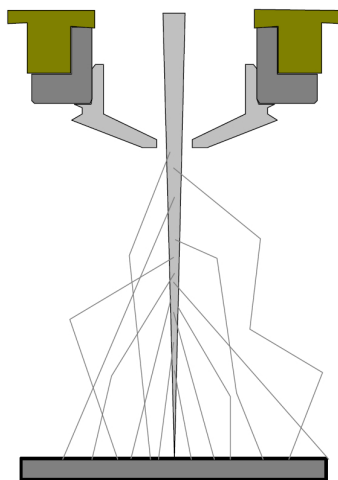

Figure 3: Schematic drawing of the scattering in an ESEM [8].

This means that the signal is generate only by those electrons, which are not scattered at all and therefore the resolution is not influenced by scattering[9]. The increase in background due to the scattered electrons combined with the decrease of the signal, since there are fewer electrons in the unscattered beam, means that the contrast of the image decreases, as the scattering increases. Eventually the unscattered beam becomes undetectable over the background of the scatter electrons and imaging becomes impossible. This is a counting experiment of how many scattering events an electron undergoes and therefore Poisson distributed [8]. The probability for no scattering event [$p(0)$] at all is:

$$p(0) = e^{-m} \tag{1}$$

where m is the average number of scattering events per electron.

The average number of scattering events per electron is given by [10]:

$$m = \frac{\sigma(U)}{k_B * T} * p * \theta \qquad (2)$$

where σ $[m^2]$ is the total scattering cross section, U $[V]$ is the acceleration voltage, k_B $[\frac{J}{K}]$ is the Boltzmann constant, T $[K]$ is the temperature of the gas, p $[Pa]$ is the pressure and θ $[m]$ is the stagnation gas thickness, which will be described in more detail below.

Therefore the portion of the beam which is unscattered is:

$$I = I_0 * e^{-m} = I_0 * e^{-\frac{\sigma(U)}{k_B * T} * p * \theta} \qquad (3)$$

where I $[A]$ is the current of the unscattered beam and I_0 $[A]$ is the total beam current.

In reality the beam does not travel through a gas with constant pressure, since there is a complicated pressure gradient between PLA 1 and PLA 2. To illustrate this point, figure 4 shows a Monte-Carlo simulation of the molecular density between PLA 1 and PLA 2 in a FEI Quanta 600 ESEM [3].
 This complicated pressure gradient is taken into account by the usage of
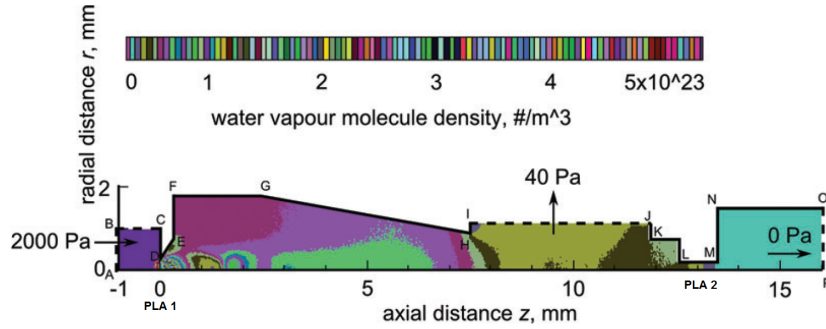
Figure 4: Monte-Carlo-simulation of the particle density between PLA 1 and PLA 2 in a FEI Quanta 600 ESEM; The chamber is to the left, the column is to the right [3].

the stagnation gas thickness, rather than the distance that the beam travels through the gas. The stagnation gas thickness can be expressed as [11]:

$$\theta = ED + \Delta \qquad (4)$$

6

where ED $[m]$ is the environmental distance, which is the distance PLA 1 to sample, which is given by $ED = WD_{sample} - WD_{PLA1}$, where WD $[m]$ is the working distance and Δ $[m]$ is the additional stagnation gas thickness.

This is a simplification that assumes that the pressure from the chamber continues constantly above PLA 1 and then immediately drops to zero after a certain distance Δ, which is referred to as the additional stagnation gas thickness in this work. Figure 5 illustrates this.
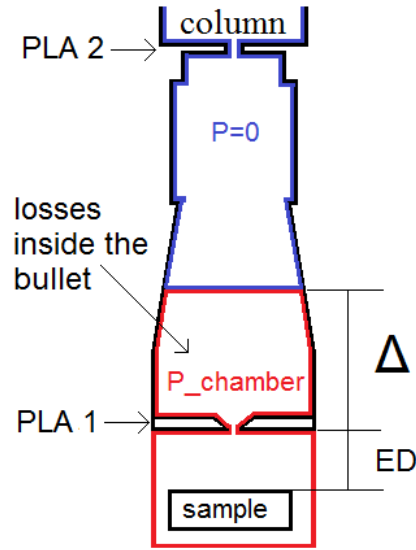
Figure 5: Schematic drawing of the simplification assumed by the stagnation gas thickness.

$$m_\Delta = \frac{\sigma(U)}{k_B * T} * \Delta * p_{chamber} \overset{!}{=} m_{PLA1}^{PLA2} = \frac{\sigma(U)}{k_B * T} * \int_{PLA1}^{PLA2} p(z)dz \qquad (5)$$

$$\Longrightarrow \Delta := \int_{PLA1}^{PLA2} \frac{p(z)}{p_{chamber}} dz \qquad (6)$$

The additional stagnation gas thickness is a very useful parameter to determine the quality of the pressure limiting system, since it contains all relevant information about the scattering between the PLAs and presents them in a way that is easy to assess for somebody with experience in environmental electron microscopy.

3.3 Secondary electron detection

Secondary Electrons (SE) are used for imaging in ESEM, because they allow for high resolution imaging[12] and their signal can easily be amplified due to the gas in the sample chamber. Additionally the positive gas ions generated by the amplification suppress charging artifacts at the surface of the sample. Figure 6 shows a schematic drawing of an SE-detector in an ESEM.
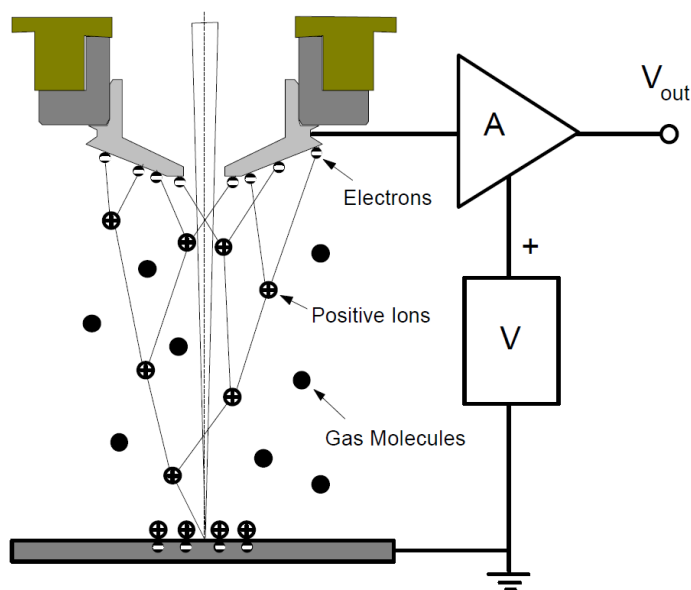

Figure 6: Schematic drawing of a SE-detector in an ESEM [8].

The SE detector is an electrode, which is biased with a couple of hundred volts. The secondary electrons, which have an energy of less than 50 eV, are accelerated towards the detector. The SE signal is amplified by collisions with the gas molecules of the imaging gas as shown in figure 6 and the current caused by the electrons from this cascade is measured at the detector and used to create an image. More sophisticated designs are also possible[13,14,15] but have only a limited advantage over this simple design. As describe in chapter 3.2, the loss of signal due to scattering is limiting the application of an ESEM. Therefore achieving the highest possible amplification in the desired pressure range is vital for high quality ESEM imaging. According to Thiel[7,16], once the electrons have undergone an initial acceleration phase just after being generated at the surface of the sample, the amplification can be describe as:

8

$$\frac{N^-(d_{gap})}{N^-(0)} = e^{\int_0^{D_{eff}} \alpha(z)*dz} \tag{7}$$

where $N^-(d_{gap})$ is the total amount of electrons collected at the detector, $N^-(0)$ is the amount of electrons starting at the sample surface, d_{gap} $[m]$ is the distance between the sample and the detector, z $[m]$ is the distance traveled from the sample surface towards the detector, $\alpha(z) [\frac{ion-pairs}{m}]$ is Townsend's first ionization coefficient and D_{eff} $[m]$ is the effective gap distance, which is taking into account the initial acceleration phase of the electrons.

Where the Townsend's first ionization coefficient is given by [17,7]:

$$\alpha(z) = \frac{P}{\lambda_1} * e^{\frac{-V_i*P}{\lambda_1} \frac{1}{\chi(z)}} \tag{8}$$

where P $[Pa]$ is the pressure, λ_1 $[mPa]$ is the mean free path of inelastic scattering of an electron at the unit pressure, V_i $[eV]$ is the ionization energy of the gas and $\chi(z)$ $[\frac{V}{m}]$ is the electric field strength.

The strength of the electric field is given by the voltage apply to the detector, the distance between the detector and the sample and the shape of the detector. The easiest way to increase the electric field is to increase the voltage. However, this increases the electric field throughout the entire sample-detector-gap, which will eventually lead to arching and make imaging impossible. Arching can be avoided by changing the gradient of the electric field rather than its overall strength. This can be done by choosing the right shape of the detector and detector-sample distance. An approach that is particularly important to ensure image quality at high pressure.

4 Measurement techniques

4.1 Single picture signal to noise ratio

In order to determine the overall quality of the detector-bullet-system and also to compare different detector designs, a matlab script was programmed which is able to determine the signal to noise ratio and the contrast of a single picture. These pictures were taken from a standardized sample under standardized conditions. Some example pictures at different SNRs can be found in the appendix 8.3.

4.1.1 Algorithm

This chapter describes the algorithm, the sample and the standardized conditions used. The source code of the algorithm can be found in the appendix 8.1.

The script is specifically designed for pictures where there is a dark background on the left side and a bright object on the right side of the picture. The sample used to achieve that is a 10 μm copper wire on a carbon-tape (figure 7).
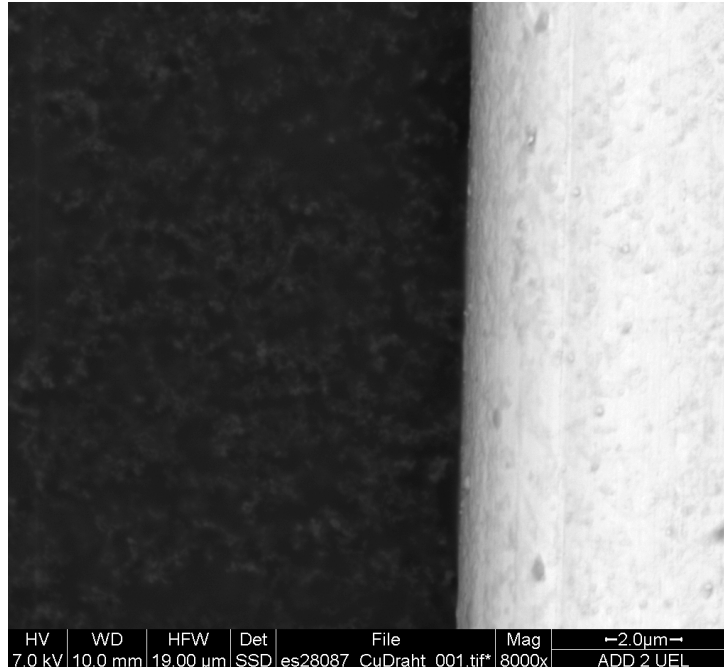

Figure 7: Example of a picture used to determine the SNR; 10 μm copper wire on carbon-tape.

In order to assure reproducible conditions the beam current has to be set to the same value in high vacuum for two pictures being compared and the contrast and brightness settings have to be used to achieve maximum contrast. The beam current is set in high vacuum using a Faraday cup (chapter 4.2.4) to measure it and the spot size and gun tilt settings of the microscope to manipulate it. It was always set to 10 nA and all SNR pictures were taken using a FEI Quanta 200 and a dwell time of 60 µs. Maximum contrast is achieved by performing a linescan across the edge of the wire and manipulating the contrast and brightness settings until the biggest possible difference between the signal from the c-tape and the copper wire is achieved. There cannot be any oversaturation or undersaturation. Figure 8 shows an example of such a linescan and illustrates how the signal is defined.
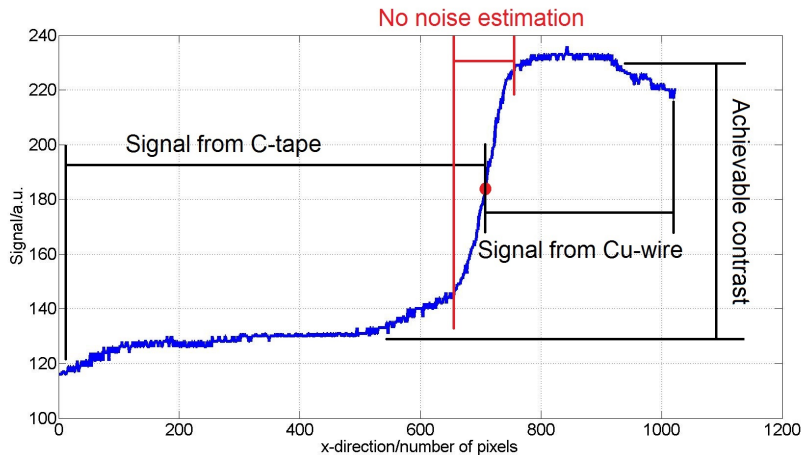

Figure 8: Example of a linescan in order to set the contrast and brightness settings to achieve maximum contrast.

The signal is now defined as the difference between the average of the bright area(copper wire) minus the average of the dark background(carbon-tape). The point where the slope is the steepest is defined as the frontier between the background and the copper wire. Everything to the left of this point is considered as background and everything to the right is considered as signal from the wire. Therefore the signal is also a measure for the maximum achievable contrast, which is important since most of the quality loss at high pressure is due to a loss of contrast rather than an increase in noise, as demonstrated by the results in chapter 5.2.2. The unit of the signal would be the gray value scale of the image, which itself is an arbitrary unit of the current at the detector. For this reason, the unit of the signal(contrast)

11

and the noise for that matter will be referred to as an arbitrary unit in this work. The noise is estimated by denoiseing the image and comparing the noiseless image with the original image. First a matlab build-in median-filter(medfilt2) is used to denoise the image. Figure 9 illustrates how this median-filter works.
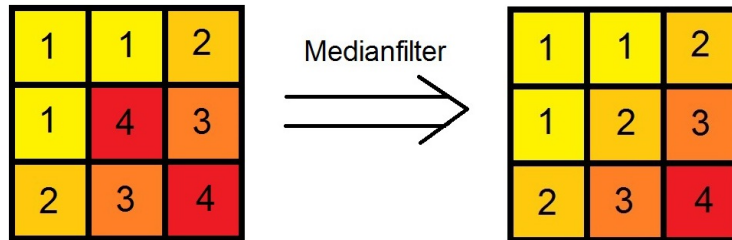

Figure 9: Illustration of how a median-filter works using 4 colors.

The median-filter selects a pixel and its 8 neighbors and then replaces the middle pixel with the median value of those nine pixels. This effectively filters white noise as long as it does not form clusters of several pixels and it does not effect features of the picture that are bigger than several pixels. Afterward, the denoised image is subtracted from the original image, which creates an image that consists only of the noise of the original image. An example of this process can be seen in figure 10.
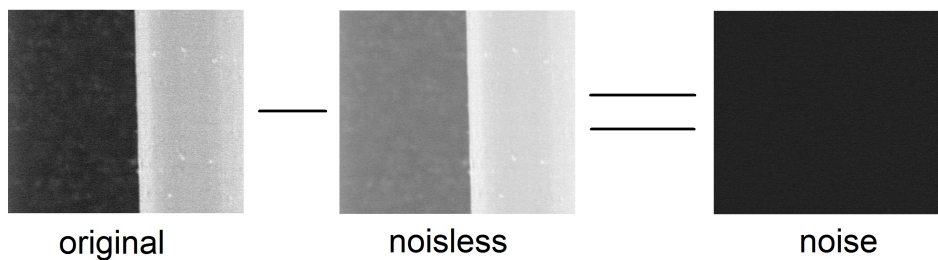

Figure 10: Example of how the noise is calculated from the original and denoised picture.

The noise is now defined as the standard derivation of this image. However, the area ± 50 pixel around the point where the slope is the steepest is excluded from the noise estimation, as indicated in figure 8. This is done because the noise might be overestimated by the median-filter in this area due to the rapid change of signal. This is a rather crude method for estimating

the noise, but it appears to be more stable for very noisy pictures then more sophisticated methods. That is especially important since the microscope is taken to its limits in this work. It is also shown in chapter 4.1.2 that this method is reasonably accurate. The SNR is, as commonly done for the SNR of an image[18], calculated in dB in this work:

$$SNR = 10 * log_{10}(\frac{Signal}{Noise})\ dB \tag{9}$$

4.1.2 Tests against artificial pictures

In order to ensure the accuracy of the matlab-script itself, it was tested against artificial pictures. Three different conditions for the loss of quality were tested:

1. A black and white picture with added white noise

2. A black and white picture with increasing loss of contrast

3. A high vacuum picture of the copper wire with added white noise

Artificial pictures: white noise

White noise is added to a black and white picture(fig.11), until the standard derivation is 100 a.u.(fig.12), which is well beyond the standard derivation of the noise in a SEM-image with a reasonable scanning time.
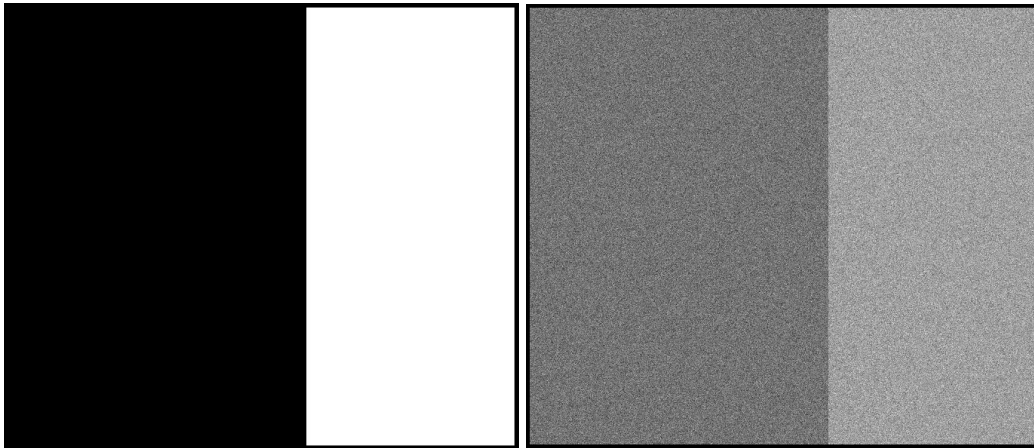

Figure 11: Black and white picture without noise.

Figure 12: The same picture as fig.11 with 100 a.u. white noise.

Fig. 13 compares the estimated SNR with the true SNR. The estimation is more accurate, if the SNR is low, but even at the highest SNR value tested, the error is only 2.4 %. The tested range covers the whole range, which can be expected in an experiment.
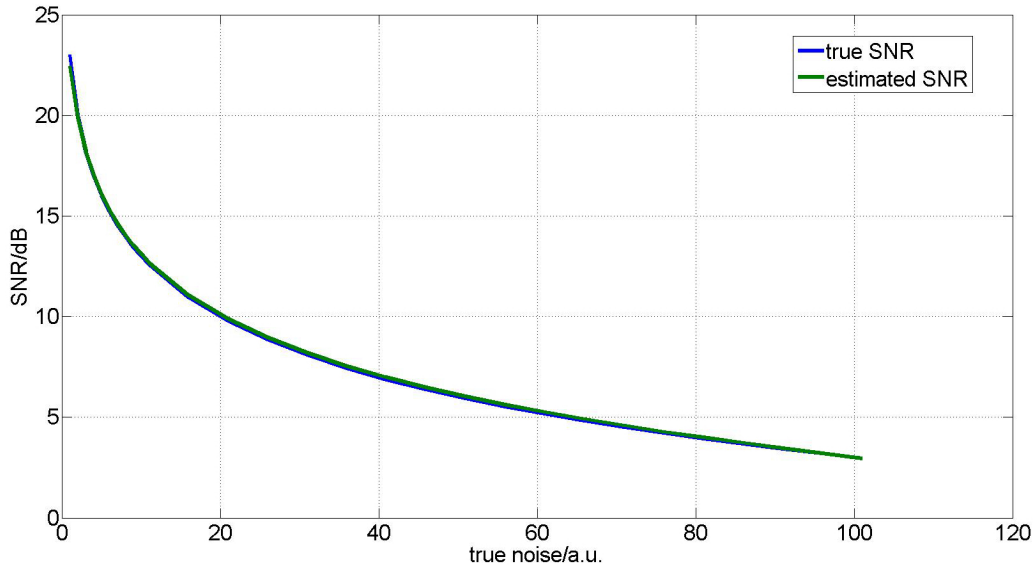

Figure 13: Estimated SNR compared with the real SNR for a black and white picture with added white noise.

Fig. 14 compares the estimated signal with the actual signal, according to our definition. Though there is a perceived loss of contrast (see figure 12) the signal remains the same, due to the mathematical structure of white noise. However, in a real electron microscope the SNR is always reduced due to a combination of white noise and loss of contrast, with the loss of contrast being the dominant factor. Therefore in a real experiment white noise with a magnitude sufficient to achieve the whole SNR-range without loss of contrast will not occur. Therefore the signal still remains a valid estimator for the maximum achievable contrast. The signal estimation works very well for small white noise and has an error of up to 7 % for high white noise, but as already explained this is not relevant for our experimental condition.
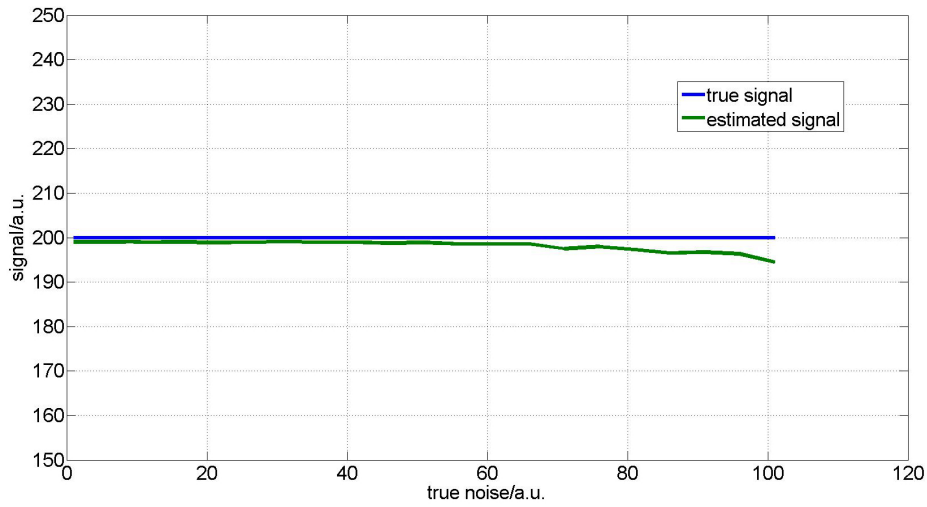
Figure 14: Estimated signal compared with the real signal for a black and white picture with added white noise.

Fig. 15 compares the estimated noise with the actual noise. The estimation works well over the entire simulated range, with a slight under estimation of the noise for very large standard derivations. However, the error is never larger than 2 %.
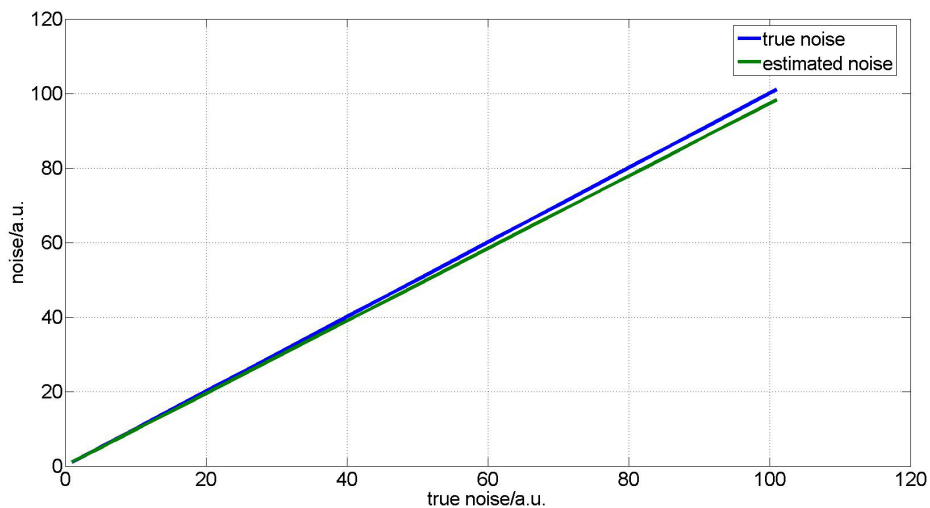

Figure 15: Estimated noise compared with the real noise for a black and white picture with added white noise.

Artificial pictures: loss of contrast

To test the algorithm for different conditions, the contrast of a black and white picture is decreased from 200 a.u.(fig.16) to 3 a.u.(fig.17). It can be seen in figure 17, that 3 a.u. is already fewer contrast than acceptable in electron microscopy and there also is a white noise of 2 a.u. in all pictures. Considering the actual measurement results in chapter 5.2.2, this test reflects the conditions in an ESEM at high pressure very well.
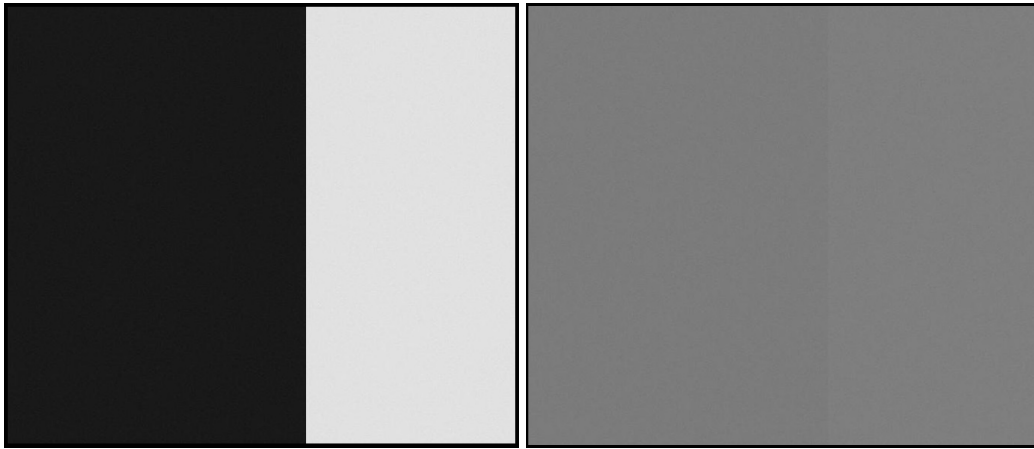

Figure 16: Black and white picture with 200 a.u. contrast and 2 a.u. white noise.

Figure 17: The same picture as fig.16 with 3 a.u. contrast and 2 a.u. white noise.
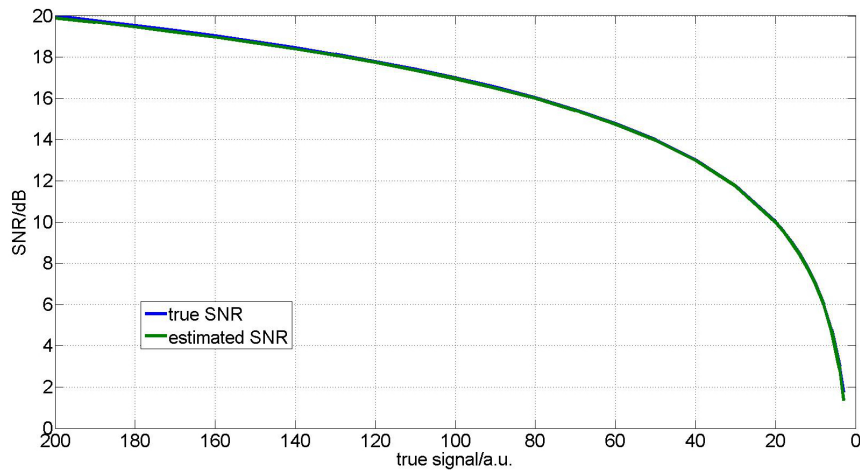
Figure 18: Estimated SNR compared with true SNR for a black and white picture with 2 a.u. white noise and increasing loss of contrast.

Fig. 18 compares the true SNR with the estimated SNR. The SNR is slightly underestimated, but the error is smaller than 1 % in the most relevant range ($\approx$15-20 dB) for ESEM. Fig. 19 compares the estimated signal with the true signal. It can be seen that the estimation works well. Just like the SNR, the signal is slightly underestimated but the error is smaller than 1% in the most relevant range for ESEM of $\approx$15-20 dB, which in this simulation is true signal $\approx$ 60-200.
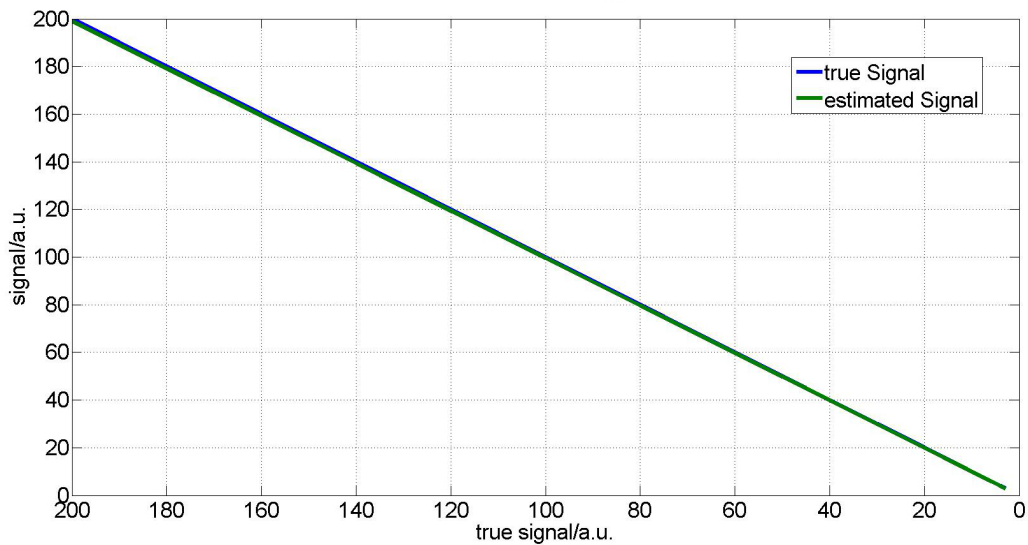
Figure 19: Estimated signal compared with true signal for a black and white picture with 2 a.u. white noise and increasing loss of contrast.

Fig. 20 compares the estimated noise with the true noise. The noise is slightly overestimated, hence canceling some of the underestimation of the signal in the SNR estimation. The error is small over the entire range (maximum 1,7 % at 200) and decreases with decreasing signal.
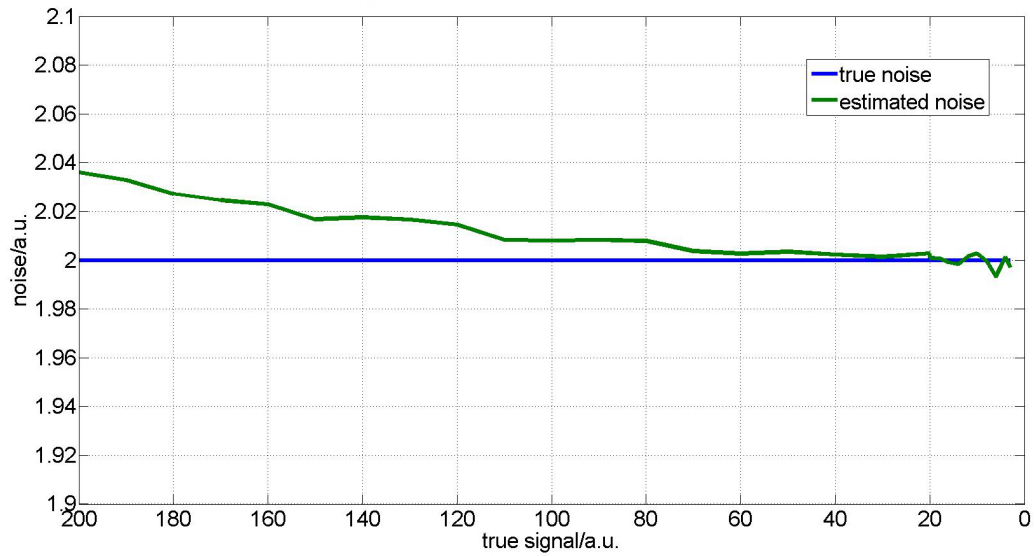
Figure 20: Estimated noise compared with true noise for a black and white picture with 2 a.u. white noise and increasing loss of contrast.

Real pictures: artificial white noise

Since a picture with one uniformly black and one uniformly white area is the ideal working condition for the algorithm, it was also tested with a high vacuum(HV) picture(fig.21) of the copper wire with up to 402 a.u. of artificially generated white noise(fig.22).
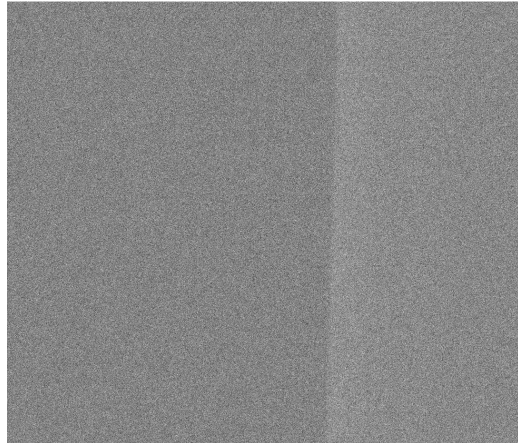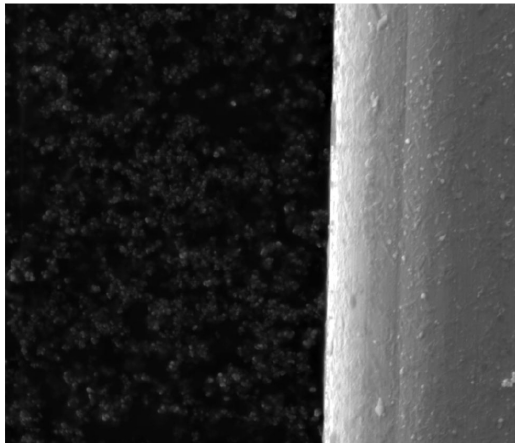
Figure 21: Original HV-picture of the copper wire.

Figure 22: HV-picture of the copper wire with 402 a.u. noise added.

Fig. 23 shows the true SNR compared to the estimated SNR. The estimation works just as well with a real picture. The SNR is being slightly over estimated. However, the largest error is only 0.13 dB.
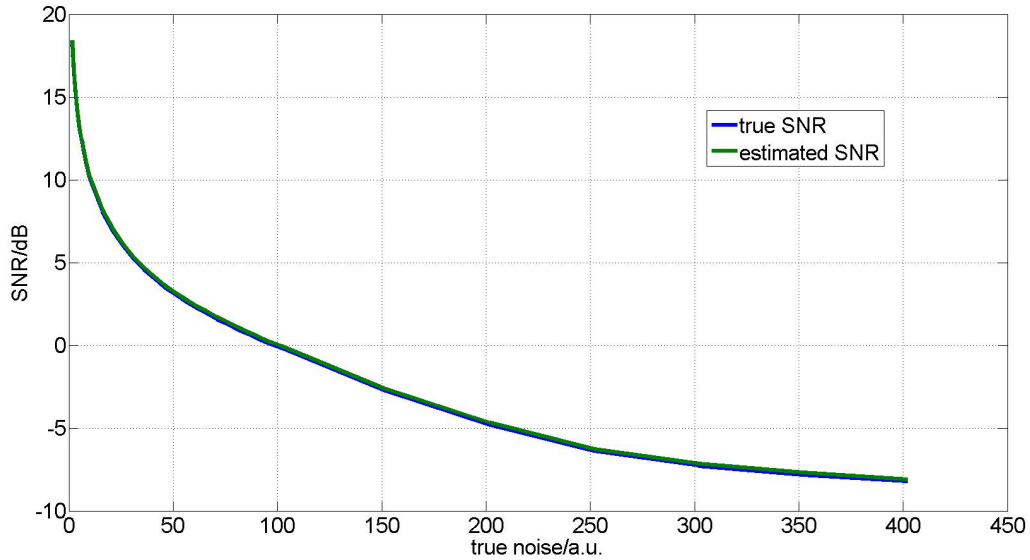
Figure 23: Estimated SNR compared with true SNR for a HV-picture of the copper wire with up 403 a.u. of white noise added.

4.1.3 Test against real pictures and error estimation

To make sure that the results are reproducible and to check how big the experimental error is, ten pictures of the copper wire were taken in HV. The beam current, the contrast and brightness settings were all reset after every picture and the wire was always moved out of frame and focus between 2 pictures. An experimental error could be introduced because the beam current is fluctuating and also because the contrast and brightness settings have to be set manually. Fig. 24 shows the results of the measurement.
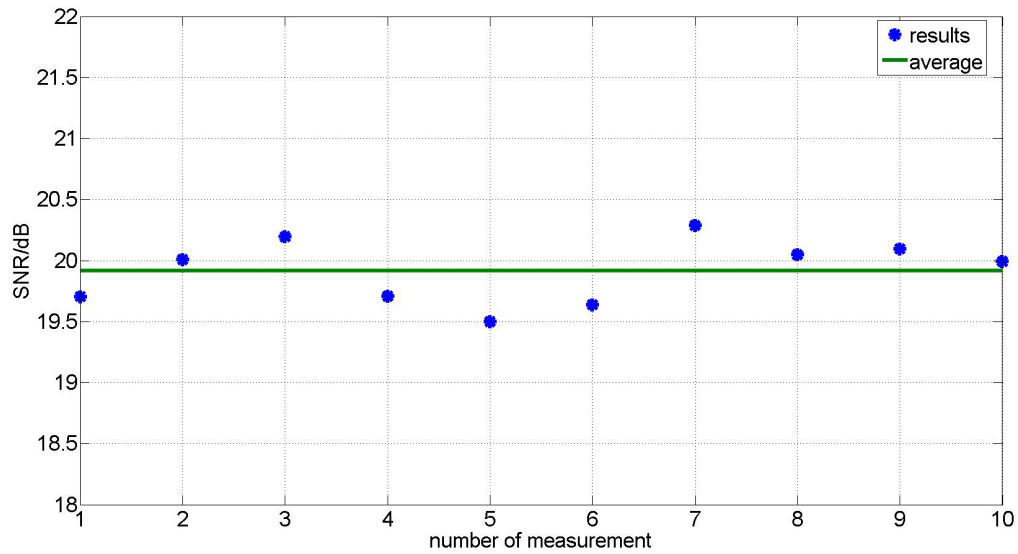
Figure 24: 10.SNR-measurements in HV in order to estimate the experimental error of the method and ensure reproducibility.

The average SNR is 19.9 dB and the standard derivation is 0.26 dB. Taking into account the systemic error of the algorithm of up to 0.13 dB, the accuracy of the overall method is ± 0.4 dB.

4.2 Beam current measurement

As described in chapter 3.2, the quality of the bullet can be quantified by determining the additional stagnation gas thickness. It follows from the equations 2, 3 and 4 in chapter 3.2 that the additional stagnation gas thickness (aSGT) can be determined by measuring $m, T, \sigma(U), p$ and ED:

$$m = -ln(\frac{I}{I_0}) = -\frac{\sigma(U)}{k_B * T} * p * (ED + \Delta) \tag{10}$$

$$==> \Delta = m * \frac{k_B * T}{\sigma(U)} * \frac{1}{p} - ED \tag{11}$$

where m is the average number of scattering events per electron, I $[A]$ is the current of the unscattered beam, I_0 $[A]$ is the total beam current, σ $[m^2]$ is the total scattering cross section, U $[V]$ is the acceleration voltage, k_B $[\frac{J}{K}]$ is the Boltzmann constant, T $[K]$ is the temperature of the gas, p $[Pa]$ is the chamber pressure, ED $[m]$ is the environmental distance, which is the distance PLA 1 to sample, which is given by $ED = WD_{sample} - WD_{PLA1}$, where WD $[m]$ is the working distance and Δ $[m]$ is the aSGT.

In order to determine m, both the unscattered and total beam current have to be measured, which is done using a special Faraday cup, as described in chapter 4.2.4, and the double spot method described in chapter 4.2.5. The temperature is held constant at 296 K by the air condition. The total cross-section is determined, as described in chapter 4.2.6. The pressure and WD are given by the microscope itself. Δ is then determined as a function of pressure by measuring m as a function of pressure for a fixed ED.

4.2.1 Measurement procedure

The beam current is measured by focusing the electron beam into a special Faraday cup, which is described in detail in chapter 4.2.3 and 4.2.4. In order to determine the average number of scattering events, knowledge of both the total beam current and the unscattered beam current is required. The total beam current is set to 1 nA. This is done by measuring the beam current in high vacuum and then setting it to 1 nA using the spot size and gun tilt controls of the microscope.
In order to ensure that the total beam current remains constant during the

measurement, the current was measured for more than 1 hour in high vacuum, after the acceleration voltage was switched on.
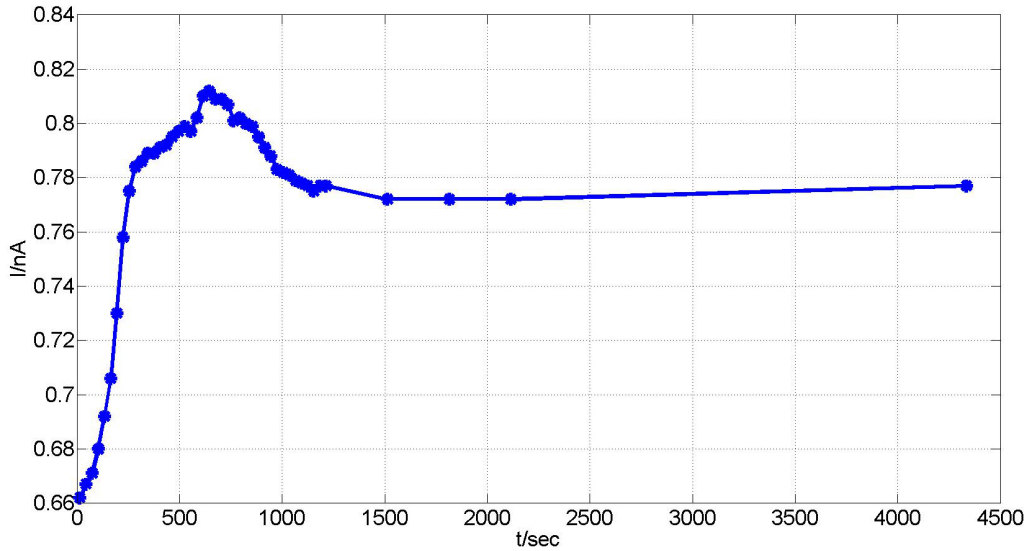

Figure 25: Beam current in high vacuum as a function of time.

The beam current strongly deviates in the first couple of minutes, but remains constant after about 20 minutes. It is therefore necessary to wait at least 20 minutes after switching the acceleration voltage on, before setting the total beam current to 1 nA. It is also possible to measure the beam current during the transition from HV to ESEM, making sure that it does not change during the transition. However, once there is gas in the sample chamber the total beam current cannot be measured anymore. It is also impossible to accurately measure it after going back from ESEM to HV, since the acceleration voltage is switched on and off automatically by the user interface. Therefore an error due to fluctuations of the total beam current cannot be excluded.

All beam current measurements were done on a FEI Quanta 600, using a Keithley 6485 picoamperemeter to measure the current.

4.2.2 Error estimation

The statistical error of the beam current measurement was estimated by performing two measurements with identical parameters that cover a range from almost 90 % to 2 % of the beam current being unscattered. Both measurements were done using the single aperture cup. These measurements

were done in the LV-Mode, where there is no PLA 1, therefore $WD = ED$ in this measurement.
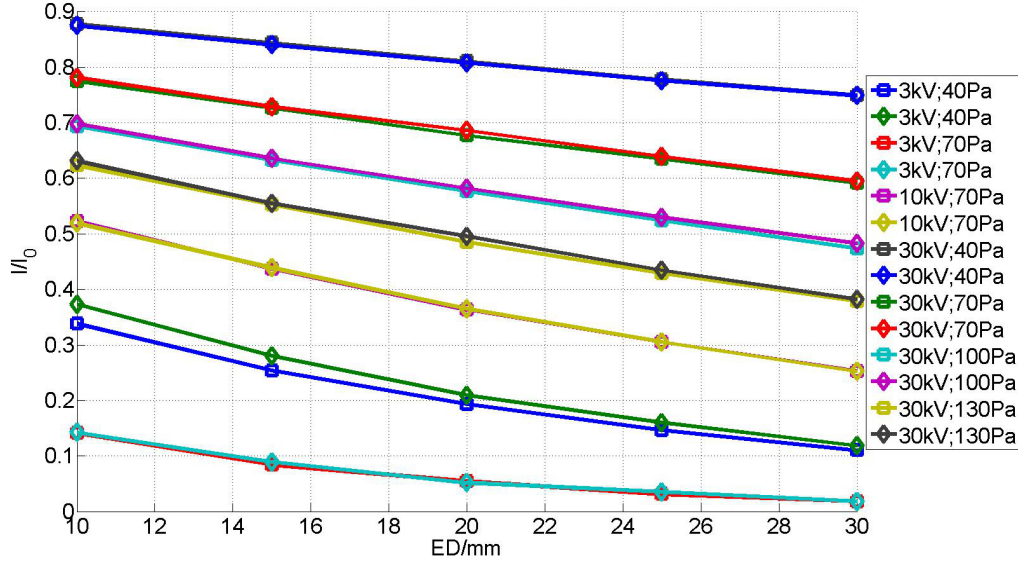

Figure 26: Measurements to estimate the statistical error of the beam current measurement using the single aperture cup.

The statistical error is now estimated by assuming that one measurement is accurate and the other includes noise:

$$\Delta \frac{I}{I_0} = std((\frac{\vec{I}}{I_0})_\Diamond - (\frac{\vec{I}}{I_0})_\Box) = 0.0078 \approx 0.01 \tag{12}$$

However, the measurements done at 3kV and 40 Pa deviate considerably more from each other than all the other measurements. This is most likely due to a shift in the total beam current. An error that, as described in chapter 4.2.1, cannot be excluded. Estimating the error from only those 2 measurements it would be 0.0107. The error estimate above is therefore rounded up to $\Delta \frac{I}{I_0} = 0.01$.

The average number of scattering events per electron(m) is calculated from the beam current using equation 10 in chapter 4.2, which means that the statistical error of m due to propagation of uncertainty is:

$$\Delta m = \left| \frac{dm}{d(\frac{I}{I_0})} \right| * \Delta \frac{I}{I_0} = (\frac{I}{I_0})^{-1} * \Delta \frac{I}{I_0} = e^m * \Delta \frac{I}{I_0} \tag{13}$$

Figure 27 shows the estimated statistical error of m as a function of m. All of the measurements to determine the aSGT inside the bullet in chapter 5.1.3 were done below m=1.4, which means that the statistical error of m in those measurements is 0.04 or less.
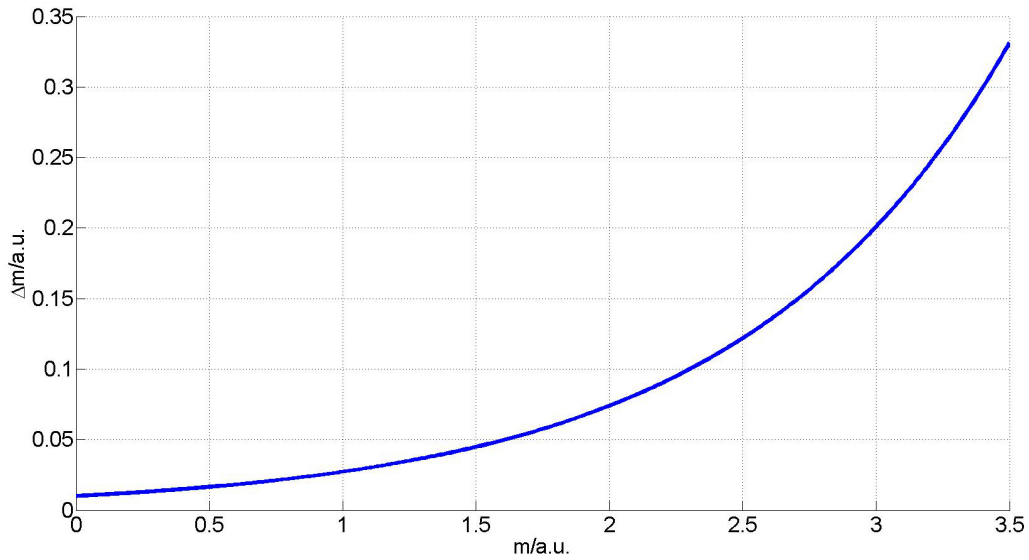

Figure 27: Estimated statistical error of the number of scattering events per electron.

The systematic error of these measurements, due to scattered electrons that still pass through the aperture of the cup, is larger. It is described in more detail in chapter 4.2.5 and also reduced by the double spot method described in that chapter. It can be estimated from the aSGT measurement in chapter 5.1.3, which puts it at up to 50 % even with the double spot method. However, this systematic error only causes a constant downwards shift of m. It does not influence the measurement of the total scattering cross-section in chapter 4.2.6, which only depends on the slope of m as a function of ED. It also does not influence the measurement comparing the single and double shielded cup in chapter 4.2.4, since in both cases the same aperture diameter was used for the shielding aperture. However, it does influence

24

the aSGT measurement in chapter 5.1.3. It can be taken into account by performing a measurement with a very small PLA 1, which can be assumed to have an aSGT close to zero.

4.2.3 Double aperture cup

In high vacuum the beam current can be measured using a simple Faraday cup. However, in an ESEM as explained in chapter 3.3, the SE-detector creates ions that are accelerating towards the sample. Those ions would create a positive current interfering with the measurement of the beam current if the Faraday cup is not modified to be shielded against them. Two possibilities to shield the cup, one using a double aperture cup and the other using a single aperture cup, were tested. Figure 28 shows a schematic drawing of the double aperture cup.
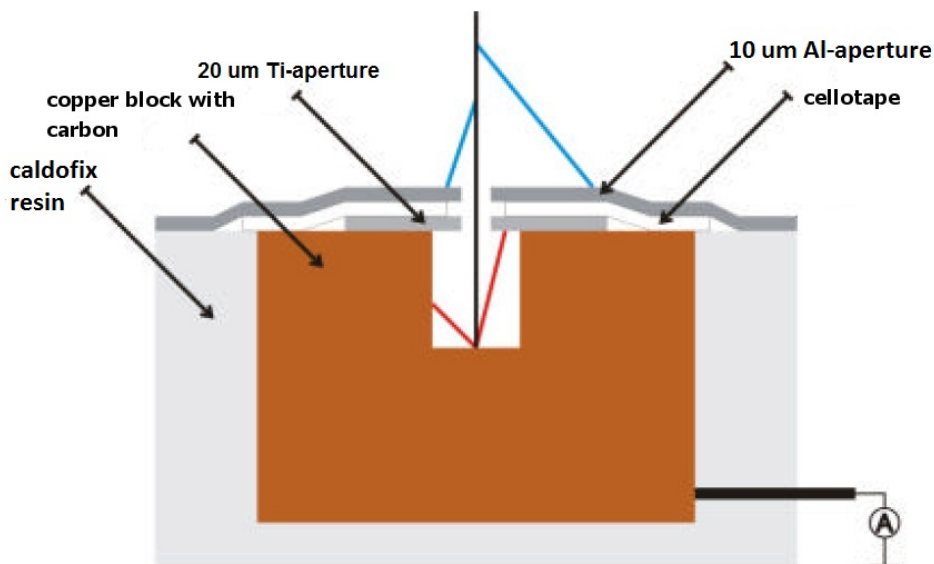
Figure 28: Schematic drawing of the double aperture cup [19].

The 10 µm Al-aperture is grounded and separated from the rest of the cup using a double sticky tape with a 3 mm hole in the middle. It therefore absorbs both the scattered electrons and the ions, generated by the SE-detector. The unscattered electrons pass through the Al-aperture and the Ti-aperture and are detected by the Faraday cup formed by the copper block with the carbon filled hole and the Ti-aperture.
This cup is rather difficult to build since the two apertures have to be aligned,

which is done by gluing an Al-foil on the Ti-aperture using a double sticky tape and then cutting the Al-aperture out of the foil using a focused ion beam microscope (FIB Nanolab Nova 200). Another drawback of this design is that it is fragile. Accidentally touching the Al-foil or even differences in temperature can cause the Al-aperture to shift slightly. Therefore a design using only one aperture was derived.

4.2.4 Single aperture cup

Figure 29 shows a schematic drawing of the single aperture cup.
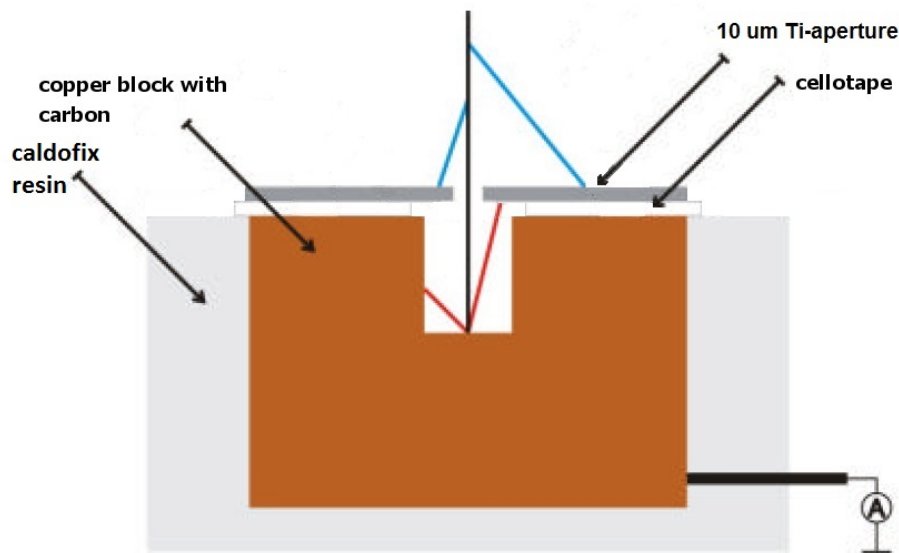
Figure 29: Schematic drawing of the single aperture cup [19].

The 10 µm Ti-aperture is grounded and separated from the rest of the cup using a double sticky tape with a 3 mm hole in the middle. No second aperture is put on top of the copper block with the carbon filled hole, which is 2 mm wide and 7 mm deep.
The drawback of this design is that some electrons, which are reflected almost straight backwards, are not detected since they hit the grounded Ti-aperture. Comparing the 2 cups in high vacuum shows that the single aperture cup measures a current which is about 5-10 % smaller than the actual current. However, we always measure a ratio of current $\frac{I}{I_0}$. If both, the beam current in high vacuum and the beam current in the environmental mode, are measured using the same cup, then the bias should cancel out. In figure 30

26

measurements done with the double aperture and the single aperture cup are compared. These measurements were done in the LV-Mode, where there is no PLA 1, therefore $WD = ED$ in this measurement.
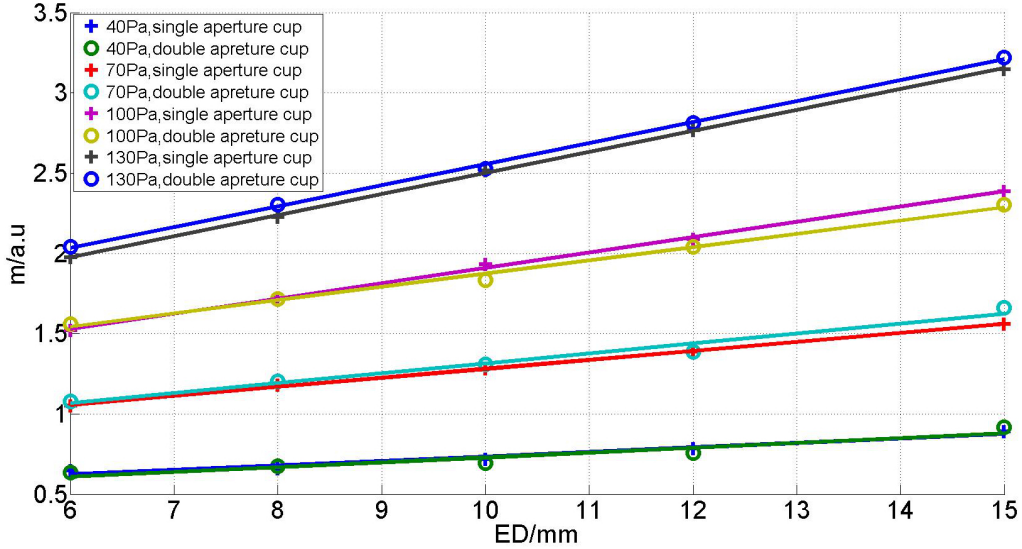

Figure 30: Average number of collision measured with the single aperture cup and the double aperture cup at U=5kV.

Both cups produce equivalent results within the error estimates given for the single aperture cup in chapter 4.2.2. Since there is a linear relation between m and ED we can estimate the accuracy of the single aperture cup relative to the double aperture cup by looking at how much they deviate from the linear fits also shown in figure 30:

$$Deviation = std(measurement\ \ results - linear\ \ fit) \qquad (14)$$

The single aperture cup deviates by 0.0124 from the linear relation, whereas the double aperture cup deviates by 0.0255. This indicates that the single aperture cup is considerably more accurate and will therefore be used for all further measurements.

27

4.2.5 Linescan vs spotscan

A systematic bias of the method of focusing the beam in the middle of the cup(single spotscan) is that electrons, which are scattered within a 5-µm-radius around the unscattered spot will still pass through the 10-µm-Ti-aperture. Therefore these electrons will be detected as unscattered electrons and the unscattered beam current will always be measured too high. In order to address this issue, the current was measured whilst the beam was scanned across the edge of the Ti-aperture [6]. This measurement was done using a labview script to control the Keithley 6485. A matlab script was implemented into the labview script in order to immediately analyze the results during measurement. Both scripts are included in the appendix 8.2. Figure 31 and 32 show an example of this type of measurement, which will be referred to as linescan measurement. An example of the double spot method later introduced in this chapter is also included in figure 31.
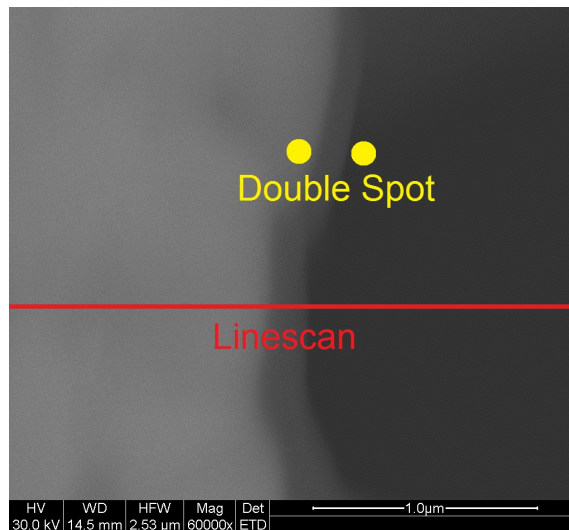
Figure 31: Example of how the linescan and double spot measurements were done.

The linescan was performed at the highest dwell time of 1.3 ms, which means that the beam takes 1.3 seconds to move from the left(outside the aperture) to right(inside the aperture) in the picture shown in figure 31. The unscattered beam current is now determined by fitting a line through the measurement outside the aperture and another line through the measurement inside the aperture, as shown in figure 32. Both are declining as more and more of the skirt falls within the aperture as the beam moves towards

the center of the cup. The unscattered beam current is the difference between the two fits in the middle of the increase in current at the edge of the aperture as indicated by the light blue line.
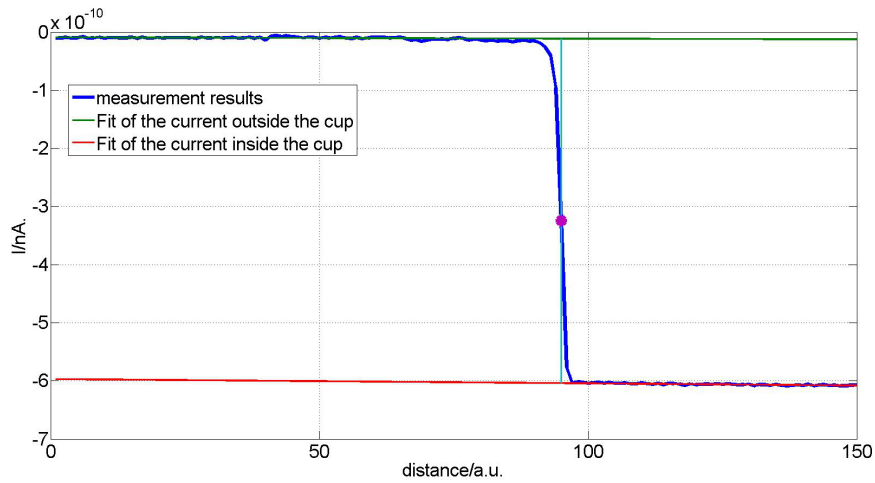
Figure 32: Example of the results and analysis of a linescan.

Figure 33 shows a comparison of the average number of collision per electron determined using the linescan and single spotscan method.
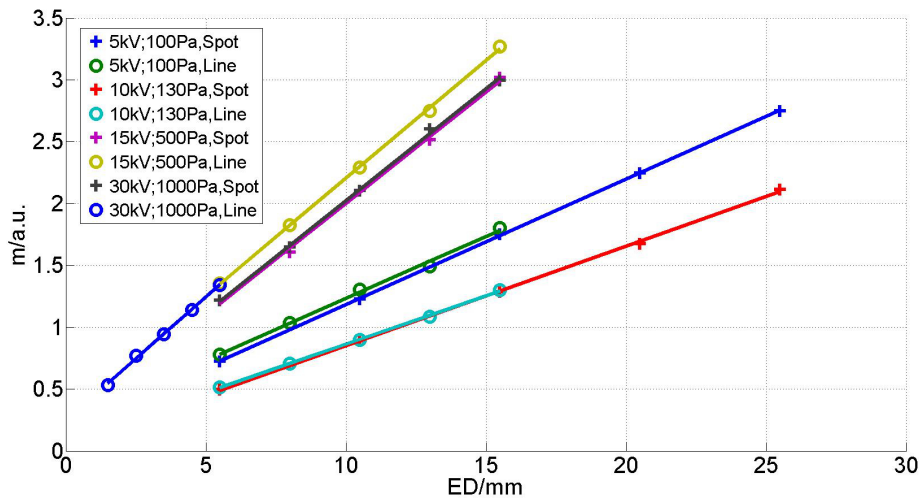

Figure 33: Linescan compared to single spotscan at various pressures, acceleration voltages and environmental distances.

As scattering increases, the difference between the results of the linescan

and single spotscan method increases. This makes sense since there are more electrons in the skirt when there is more scattering. Equivalent results to the linescan method can be obtained by taking two spot measurements, one just outside the aperture the other just inside the aperture, as shown in figure 31. The current from the spot measurement outside the cup is then subtracted from that inside the cup to determine the unscattered beam current. This measurement method will be referred to as double spot measurement. The linescan and double spot method are compared in figure 34.
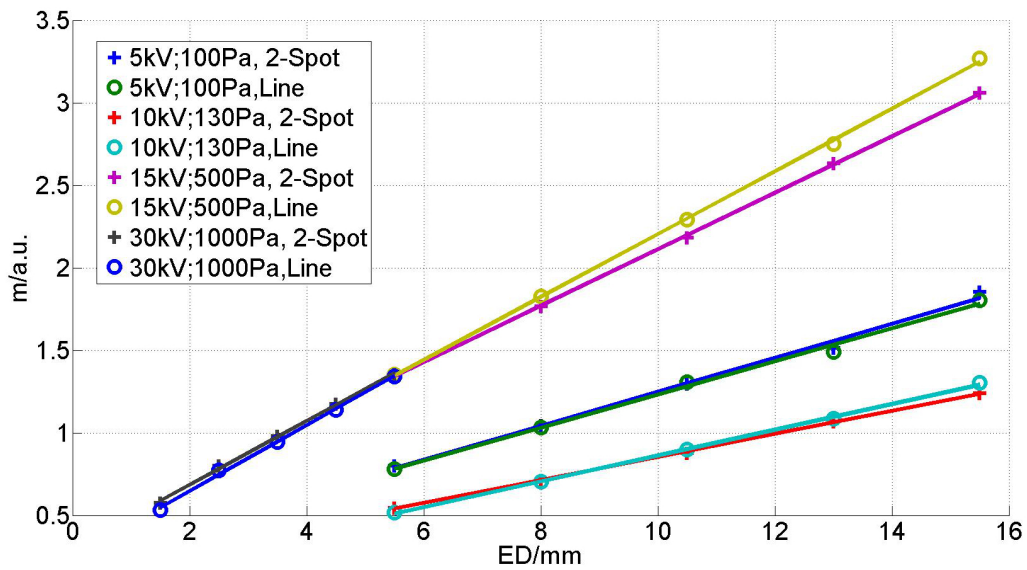

Figure 34: Linescan compared to double spot method at various pressures, acceleration voltages and environmental distances.

Both methods produce equivalent results within the error estimation given in chapter 4.2.2. The increasing difference seen at 15 kV and 500 Pa is due to the fact that as image quality decreases it becomes more and more difficult to aim at a spot just inside or outside the cup. However, all measurements to determine the aSGT in chapter 5.1.3 have been done below m=1.4, which means that this difference is irrelevant to those results. The accuracy of the two methods relative to each other was estimated the same way as describe in chapter 4.2.4, where the single and double aperture cup are compared. The deviation of the linescan method is 0.0162 and that of the double spot method is 0.0157, which indicates that both methods are about equally accurate in terms of statistical noise. Therefore the simpler double spot method was chosen for all further measurements.

4.2.6 Electron scattering cross-section

The scattering cross-section can be determined using equation 2 given in chapter 3.2:

$$m = -\frac{\sigma(U)}{k_B * T} * p * (ED + \Delta)$$

The temperature is always 296.15 K, therefore $\sigma(U)$ can be determined by measuring m for several ED at the same pressure and fitting a line to those measurements. The slope of this line is then used to determine $\sigma(U)$:

$$m = k * ED + d \tag{15}$$

$$k = -\frac{\sigma(U) * p}{k_B * T} \tag{16}$$

$$=> \sigma(U) = -\frac{k * k_B * T}{p} \tag{17}$$

Since Δ only depends on the pressure gradient inside the bullet, see chapter 3.2, it is sufficient to determine $\sigma(U)$ for one acceleration voltage which is then used for all measurements of Δ. The acceleration voltage chosen is 30 kV, because with low acceleration voltages it can become difficult to perform the measurement at high chamber pressures. The error of the measurement increases as m increases and using 30 kV minimizes the number of scattering events. Figure 35 shows the measurements used to determine σ for water vapor and figure 36 shows the measurements used to determine σ for ambient air. In order to reduce the error, the average of several measurements at different pressures was taken.The total cross-sections determined from those measurements are:

$H_2O : \sigma_{30kV} = (8.3 \pm 0.6) * 10^{-22} m^2$

$Ambient\ air : \sigma_{30kV} = (1.05 \pm 0.03) * 10^{-21} m^2$

These are comparable to those determined by Rattenberger[19] with a similar method but using a double shielded cup:

$H_2O : \sigma_{30kV} = 8.05 * 10^{-22} m^2$

$Ambient\ air : \sigma_{30kV} = 1.16 * 10^{-21} m^2$
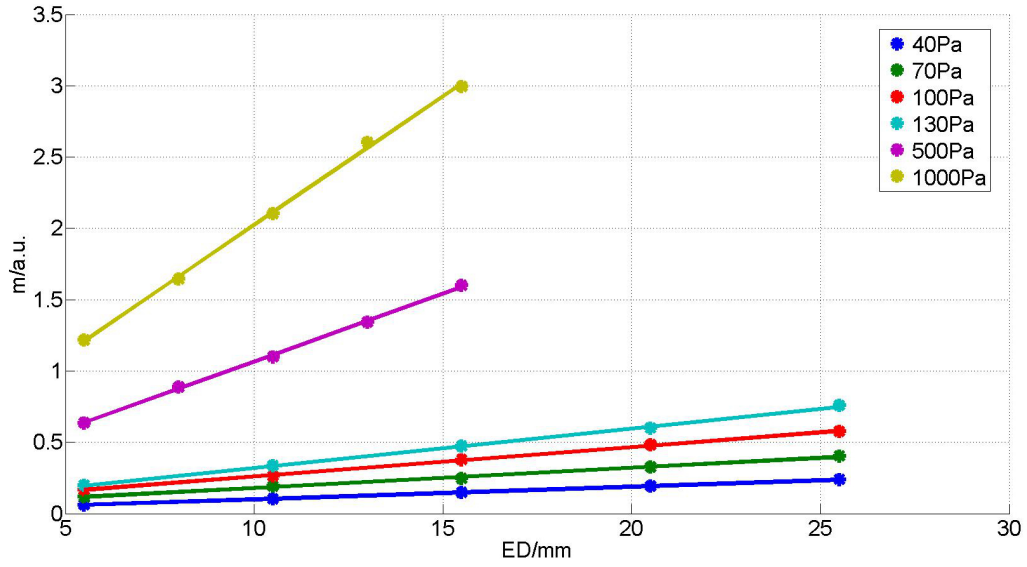
Figure 35: Measurements and fits to determine σ of water vapor at 30 kV.
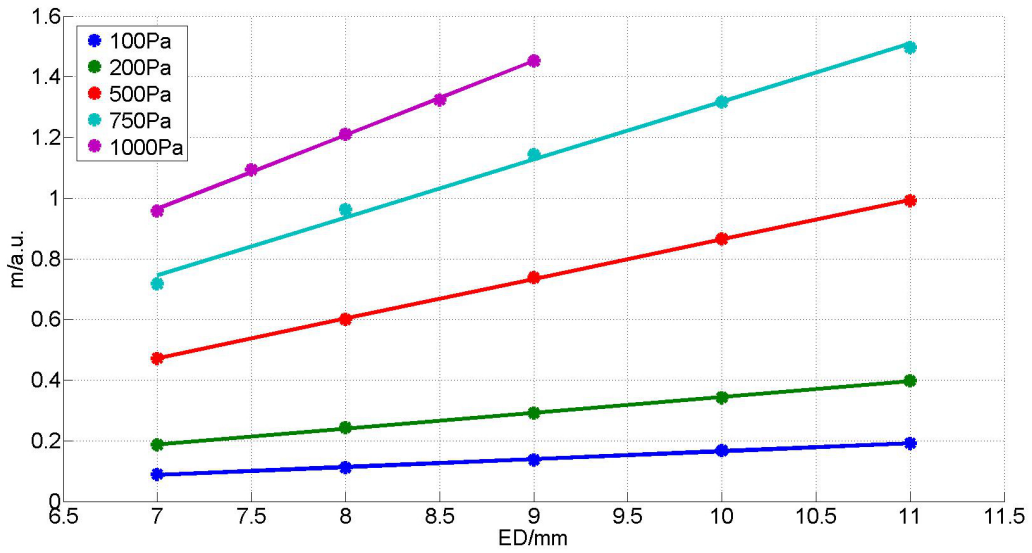
Figure 36: Measurements and fits to determine σ of ambient air at 30 kV.

4.3 Backpressure

A simple and fast way to determine the quality of the bullet is to measure the pressure at the pump exit of the EC 1. This is about where G5 is in figure 1. This pressure will be referred to as backpressure[3] in this work. Figure 37 and 38 show a picture and a schematic drawing of the experimental setup.
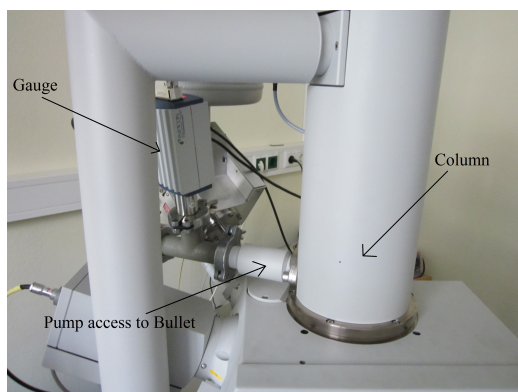

Figure 37: Picture of the experimental setup to measure the backpressure.
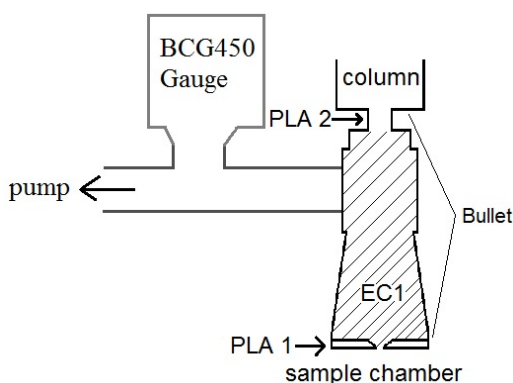
Figure 38: Schematic drawing of the experimental setup to measure the backpressure.

Measuring the pressure in one point relatively far away from the PLA 1 obviously ignores the complicated pressure gradient between PLA 1 and PLA 2. However, it still allows a qualitative measurement, since less backpressure also means less average pressure throughout the entire pressure gradient, provided that the shape of the gradient does not change too dramatically. Another advantage of this measurement, besides being simple, is that the electron gun does not have to be switched on to do it. It can be used to assure that a new design sufficiently reduces the pressure in EC 1 to protect the column, without risking damage to the gun. All backpressure measurements were done using a FEI Quanta 200 and an Inficon BCG450 gauge.

4.4 Field of view

The field of view is measured by taking a picture in high vacuum as shown in figure 39.
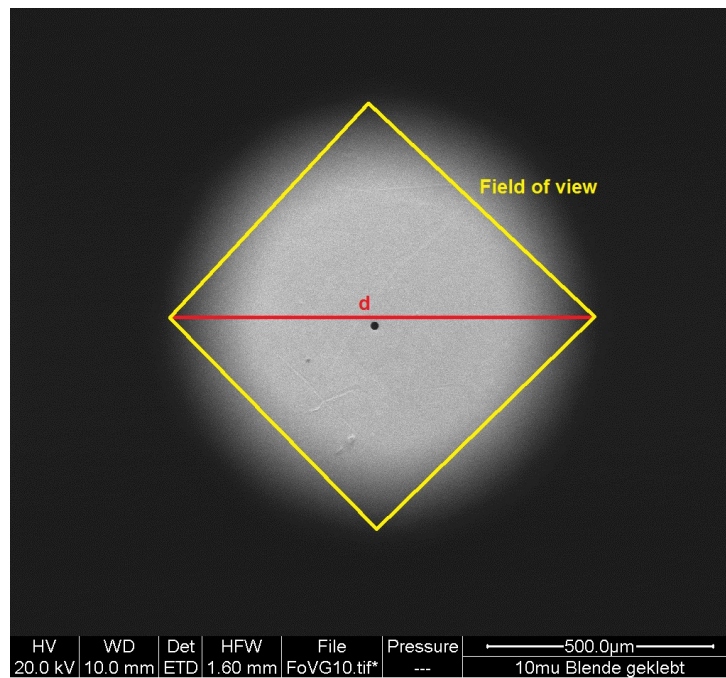

Figure 39: Example of how the field of view is measured.

The diameter of the visible circle(d) is measured, rather than the field of view itself, because it is easier to determine, which produces more accurate results. The field of view can easily be calculated with:

$$Field \ of \ view = \frac{d}{\sqrt{2}} \tag{18}$$

5 Modifications and results

5.1 Bullet

A new bullet, which allows the usage of different PLA 1 diameters, was designed. Making the PLA diameter smaller will decrease the aSGT and therefore improve image quality, but also reduced the field of view. Being able to use different PLA diameters rather than the fixed 500 µm diameter of the original design, makes it possible to achieve a far better balance of image quality and field of view for almost all applications.

5.1.1 Modifications

Figure 40 shows a schematic drawing of the original FEI design of the bullet and the bottom of the pole piece.
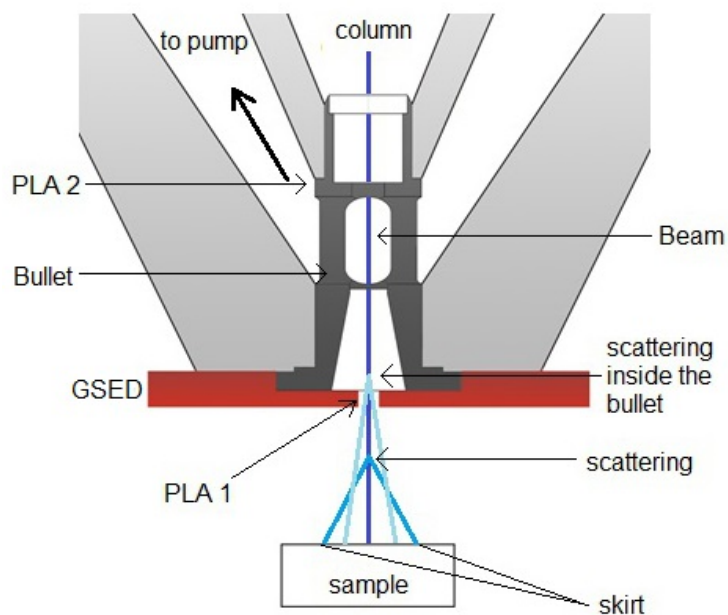
Figure 40: Schematic drawing of the original FEI design.

Only PLA 2 is position inside the bullet, whereas PLA 1 is integrated into the gaseous secondary electron detector (GSED). PLA 1 has a diameter of 500 µm and cannot be changed since it is part of the GSED. This means that the GSED has to be positioned at the bottom of the pole piece, which making it impossible to use the standard FEI solid state detector (SSD) for backscatter electrons. Furthermore, the ED is always the same as the sample-detector

distance a disadvantage discussed in more detail in chapter 5.2. PLA 2 is realized by either a 200 µm aperture (Quanta 200) or 3 consecutive 400 µm apertures (Quanta 600).

A new bullet is design were both PLAs are positioned inside the bullet. Figure 41 shows a blue print of the original and new bullet. Pictures of the two bullets can be found in the appendix 8.4.

Figure 41: Blue print of the original (right) and new bullet (left), all measures are given in mm.

The top part of the bullet is unmodified and the same PLA 2 setup is used as in the Quanta 600. At the bottom of the bullet the cone shape inside the bullet is replaced by a straight tube. The original design uses the cone shape in order to provide a bigger field of view in the high vacuum and low vacuum mode where there is no PLA 1. This is irrelevant to the new design since it is primarily designed for the ESEM mode and according

to Danilatos [3] a straight shape provides a better pressure gradient for the beam transfer. At the bottom of the bullet an additional structure similar to that holding the PLA 2 is added. This structure can hold different apertures serving as PLA 1, which are either glued in or held in place by a snap ring. This enables the use of thinner apertures than 0.8 mm, which according to Danilatos [4] should provide a better pressure gradient at the same diameter. Additionally, apertures with arbitrary diameters can be used, which allows a better balance of image quality and field of view for almost all applications than the original 0.5 mm apertures. Overall, the new setup is shorter than the original one. In this design the PLA 1 is positioned 3.3 mm below the bottom of the pole piece compared to the original design with a distance of 4.5 mm.

5.1.2 Reduced backpressure

For the backpressure measurements an Inficon BCG 450 gauge was used. Unfortunately it has an error of 15 % in the desired pressure range and it produces an additional error when measuring water vapor due to the fact that it is calibrated for air. The calibration factor given in the manual for water vapor is an average value over a pressure range of several orders of magnitude. Nevertheless, the BCG 450 is the ideal gauge for measurements in the ESEM, because it can be used for pressures form high vacuum to atmospheric pressure. The Inficon BCG 450 was tested against the more accurate Pfeiffer CMR 272 capacity gauge that controls the pressure in the sample chamber of the ESEM. Figure 42 shows the results.
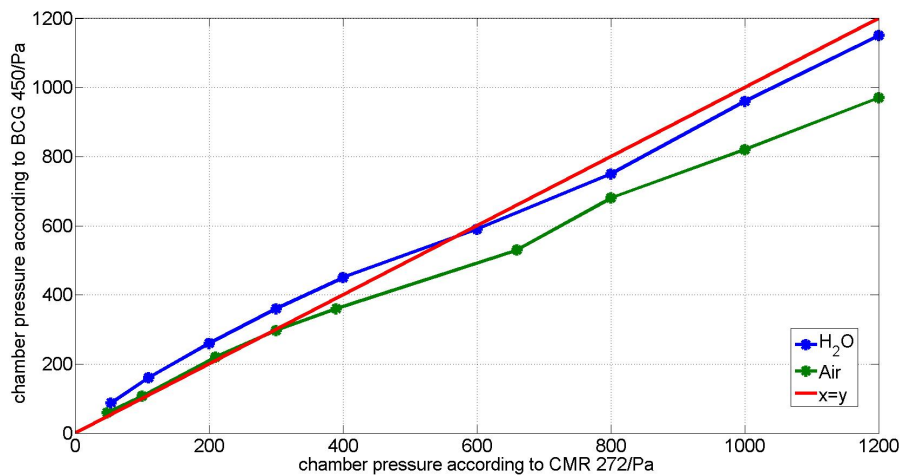

Figure 42: Test of the BCG 450 against the CMR 272.

37

The BCG 450 uses different senors at different pressure ranges. 100 to 1000 Pa is the range where the crossover from a capacitance diaphragm sensor to the Pirani sensor takes place. The Pirani sensor is used in the pressure range seen in the backpressure measurements. The measurements for ambient air are way off at high pressures but approximately lie within the 15 % boundaries once the Pirani sensors regime is reached. The measurements for water vapor are fairly accurate at high pressures but, as expected, have a higher error than the measurement using ambient air once the Pirani sensors regime is reached. An error of more than 15 % means that the absolute values given in the measurements below are only of limited quality. However, the reproducibility of the measurements is much better than a 15 % error and the backpressure measurement can provide qualitative analysis of the pressure limiting system. The quantitative analysis is done using the aSGT measurement in chapter 5.1.3. The measurements were mostly performed to see the influence of the PLA 1 diameter on the backpressure, and to control the pressure conditions for a save start-up of the electron gun. Figure 43 shows the results of a backpressure measurement preformed as describe in chapter 4.3, using different PLA 1 diameters.
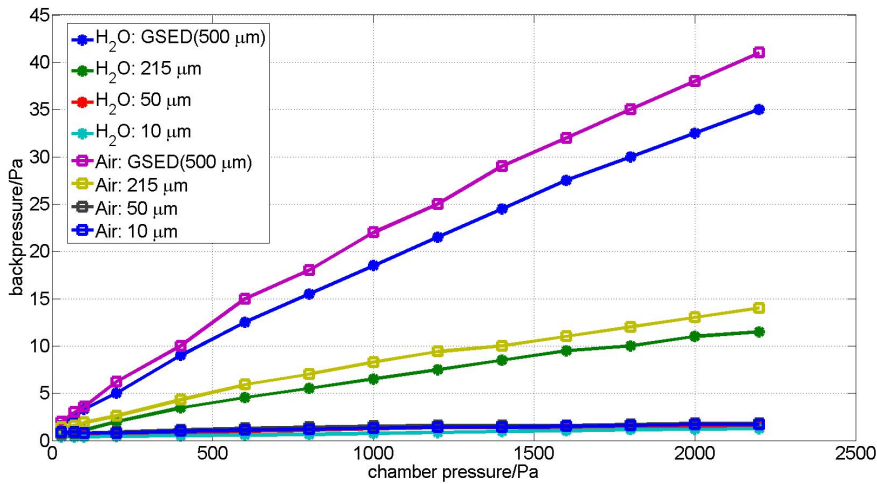

Figure 43: Backpressure for different PLA 1 diameter as a function of the chamber pressure.

The results show that the new bullet does not cause any major leakages. Making the PLA 1 diameter smaller reduces the backpressure as would be expected. However, there is no significant difference between the 50 and 10 µm PLA, which indicates that a leakage of the order of magnitude of tens

of µm PLA-diameter exists. All PLAs were held in place with a circlip in this measurement and a little mismatch of this circlip might cause a leakage. Therefore the PLAs were glued into the bullet with an in acetone well soluble Loctite 435 in the next measurement. Figure 44 shows the results of the measurements with the glued-in PLA compared to the ones which are secured with a circlip.
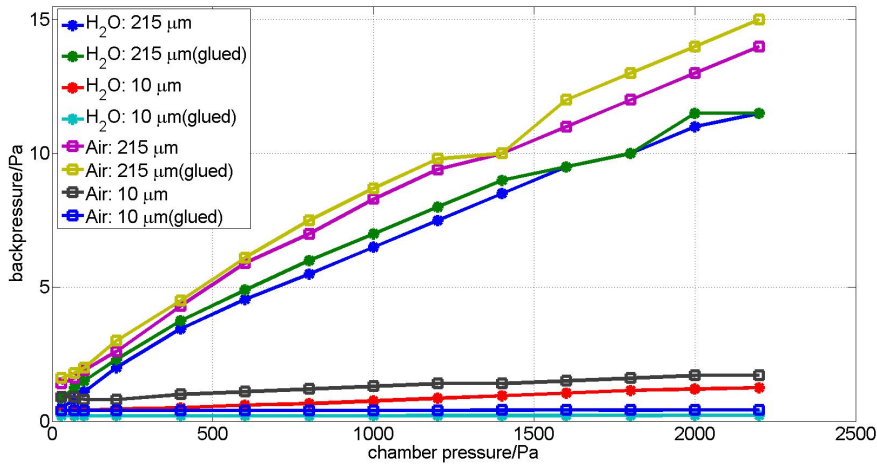

Figure 44: Backpressure as a function of chamber pressure comparing glued-in PLAs vs PLAs secured with a circlip.

The performance of the 10 µm PLA is significantly better when the PLA is glued-in. The backpressure is virtually independent of the chamber pressure when the glued-in 10 µm PLA is used. This indicates that most of the gas atoms and molecules measured with the glued-in 10 µm PLA are not caused by the gas flow from the sample chamber but rather the overall leakage of the entire pumping system. The performance of the 215 µm PLA is not influenced significantly by gluing it in. In fact the glued-in PLA performs slightly worse in this case. This indicates that the benefits of gluing the PLA in are limited to fairly small PLA diameters as would be expected of a leakage at the order of magnitude of tens of µm. In general it should be sufficient to secure PLAs bigger than 200 µm with a circlip but in order to keep the measurements as consistent as possible all PLAs in the aSGT measurements in the next chapter were glued-in.

5.1.3 Reduced additional stagnation gas thickness

The best parameter to quantify the entire pressure limiting system is the additional stagnation gas thickness (aSGT) described in chapter 3.2 [4]. It is measured as explained in chapter 4.2. The measurements were performed using an acceleration voltage of 30 kV, an ED of 2.5 mm (GSED) and 2.7 mm (all the others), apertures with a diameter of 30, 100, 200, 215 and 500 µm as PLA 1 and water vapor and ambient air as imaging gas. Figure 45 shows the results for both imaging gases and the GSED as well as 500, 200 and 30 µm aperture diameter. The other diameters have been left out in order not to overload the figure. They are included in figure 46 and 47, which show the results for any gas individually.
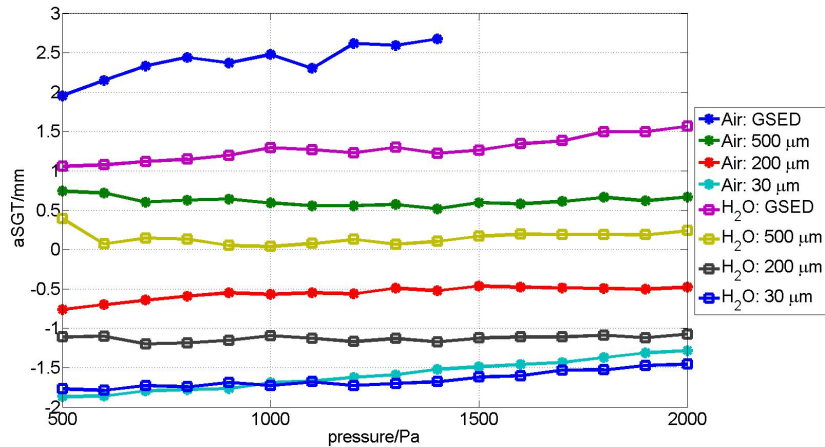

Figure 45: aSGT as a function of pressure for various PLA 1 diameters.

For PLA 1 diameters of 200 µm or smaller the aSGT becomes negative, which is impossible. This is due to scattered electrons falling within the aperture of the faraday cup as mentioned in chapter 4.2, which leads to a too high measurement of m and therefore a too low measurement of the SGT and aSGT. According to theoretical considerations of Danilatos [4] water vapor should perform better than air, which is confirmed for all PLA diameters except for the 30 µm PLA where the difference is hardly measurable. This indicates that the aSGT is close to zero for the 30 µm PLA. The systematic error mentioned above is therefore addressed by assuming that the measurement using the 30 µm PLA has an aSGT of zero and scaling the other measurements accordingly. Figure 46 shows the results for water vapor.
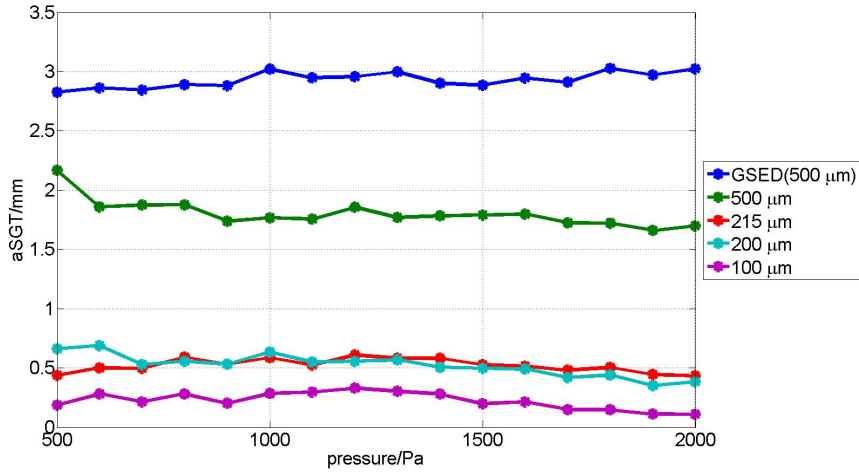
Figure 46: aSGT as a function of pressure for water vapor and various PLA diameters, assuming that the aSGT of the 30 µm PLA is zero.

The 500 µm PLA, which has the same size as the PLA built-in the GSED, has a significantly smaller aSGT than the GSED. There are three possible reasons. First off, as mentioned in chapter 5.1.1, the straight shape inside the new bullet provides a better pressure gradient according to Danilatos [3]. Secondly, the new bullet is shorter than the original design by 1.2 mm. And thirdly the PLAs are thinner than in the original design. The 500, 200, 100 and 30 µm PLAs are 250 µm thick, the 215 µm PLA is 50 µm thick and the built-in PLA of the GSED is 800 µm thick. According to Danilatos [4] thinner PLAs provide a better pressure gradient, which might also contribute to the advantage of the 500 µm PLA. However, there is no difference between the 215 µm and the 200 µm PLA indicating that the effect of reducing the thickness of the PLA from 250 to 50 µm has about the same effect as reducing the diameter of the PLA by 15 µm.
The 200 µm and 215 µm PLA improve the aSGT significantly by about 1.3 mm compared to the 500 µm PLA and 2.5 mm compared to the GSED. The 200 µm PLA already achieves about 80 % of the improvement over the GSED that is possible using a 30 µm PLA. Making the PLA smaller than 200 µm has only limited effect on the image quality whilst the field of view is significantly smaller as describe in chapter 5.1.4. Figure 47 shows the same measurement using ambient air as imaging gas.

41
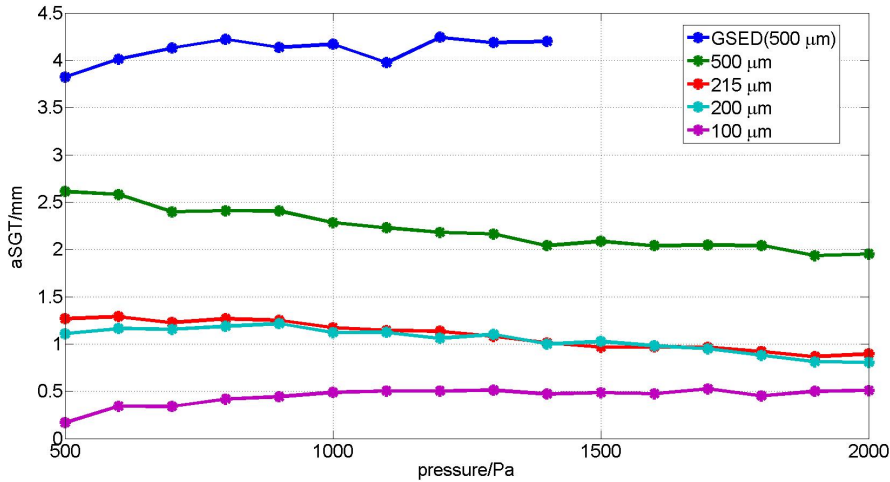
Figure 47: aSGT as a function of pressure for ambient air and various PLA
diameters, assuming that the aSGT of the 30 μm PLA is zero.

The results are similar to those using water vapor. The 500 μm PLA is
already a significant improvement over the original design. About 75 % of
the possible improvement using the 30 μm PLA is achieved using the 200 μm
PLA. There is again no measurable difference between the 200 μm and 215
μm PLA.

However, there is still room for improvements that has nothing to do with the
physics involved. Both the Quanta 200 and 600 restrict the closest focusing
distance to 4.5 mm in the ESEM-Mode, because the PLA 1 of the GSED is
at 4.5 mm. The PLA 1 of the new design is 3.3 mm below the pole piece,
meaning that 1.2 mm of the advantage gained by the new setup are lost
because the beam cannot be focused on a point closer than 1.2 mm to the
PLA 1. This is purely a restriction imposed by the software of the microscope,
since focusing the beam at a working distance of 1 mm is possible both in
the high and low vacuum mode of the ESEM. Because there is no drawback
in putting the sample as close as possible to the PLA 1, the design proposed
in this work could be significantly improved upon if the software limitations
of the working distance could be lifted.

5.1.4 Field of view

The drawback of using an aperture with a small diameter as PLA 1 is the
decrease in field of view. A measurement of the field of view (FoV) as a
function of the PLA 1 diameter (d_{PLA}) and ED was performed as described

42

in chapter 4.4 for both the Quanta 200 (thermionic gun) and Quanta 600 (field emission gun). Figure 48 shows the results for the Quanta 200.
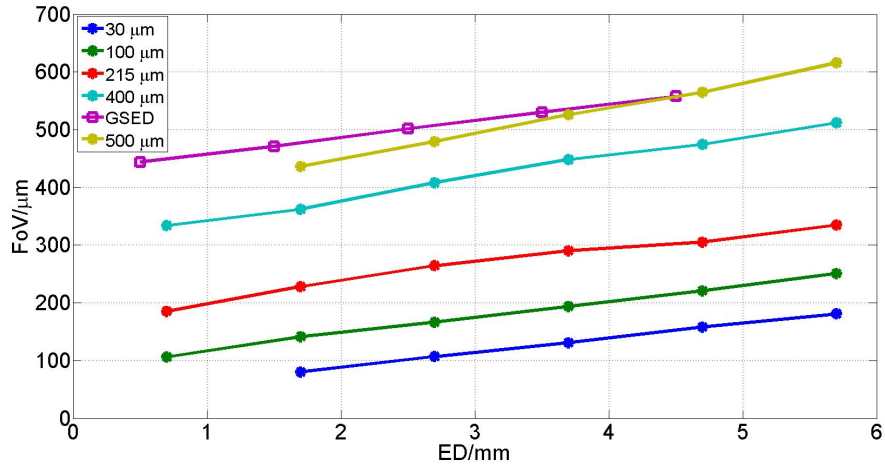

Figure 48: FoV as a function of ED for different d_{PLA} using the Quanta 200.

The FoV increases linearly as a function of both the ED and d_{PLA}. It increases faster with increasing ED than in the original design (GSED: d_{PLA}=500 µm), because the PLA 1 is closer to the pole piece in the new design. It is also notable that even with a 30 µm aperture a FoV of 100-200 µm is possible. A good compromise is the 215 µm aperture. It provides about 75 % of the advantage that the 30 µm aperture has over the GSED in terms of aSGT and has a FoV about half of that of the GSED. An empirical formula for the FoV of the Quanta 200 can be determined:

$$FoV[\mu m] = (0.04 * d[\mu m] + 23) * ED[mm] + \frac{d[\mu m]}{\sqrt{2}} + 18 \qquad (19)$$

The same measurement has been done using the Quanta 600. Figure 49 shows the results.

43
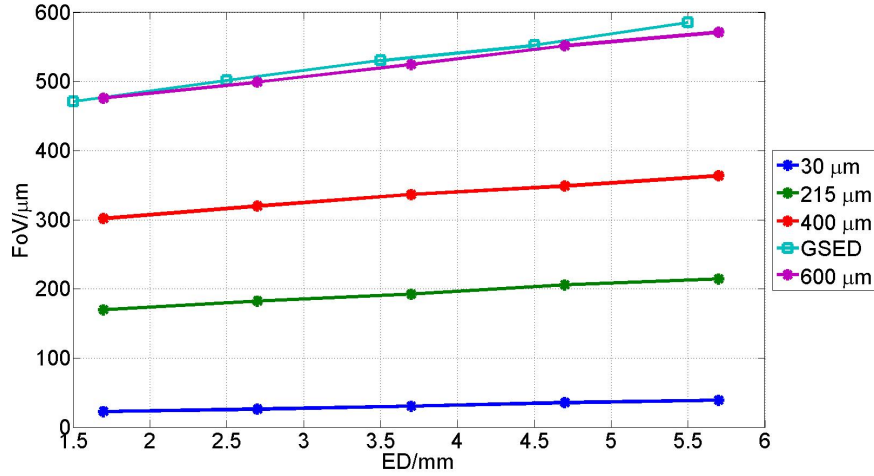
Figure 49: FoV as a function of ED for different d_{PLA} using the Quanta 600.

The results are similar to those of the Quanta 200. The field of view is again linearly dependent on the ED and d_{PLA}. The different electron optics due to the field emission gun dramatically decreases the dependents of the FoV on the ED. The GSED has a comparable FoV to the slightly bigger 600 µm aperture. Due to the decrease in dependents on the ED, the FoV of the 30 µm aperture is only about 30 µm making it considerably harder to use than in the Quanta 200. The 215 µm aperture still is a good compromise with a FOV of about 200 µm. An empirical formula for the FoV of the Quanta 600 was determined as well:

$$FoV[\mu m] = (0.035 * d[\mu m] + 3.3) * ED[mm] + \frac{d[\mu m]}{\sqrt{2}} - 9 \qquad (20)$$

For the Quanta 200 the FoV is bigger than d_{PLA} in most cases. For the Quanta 600 the FoV depends less on the ED and therefore the diameter of the FoV is about the same as d_{PLA} for most cases but it still can be bigger than d_{PLA} at larger EDs. The FoV can be bigger than the aperture size because of the focusing mechanisms in electron microscopy (see figure 50). Figure 50 also explains the gradient in illumination at the edge of the FoV.

44
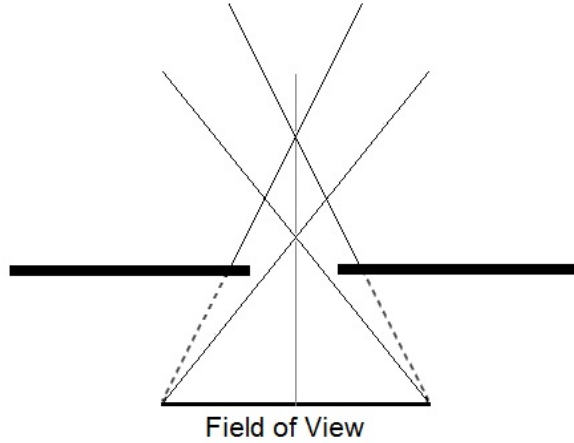
Figure 50: Scheme of the illumination in scanning electron microscopy.

Since the FoV for the Quanta 200 depends more on the ED than that of the Quanta 600, the Quanta 200 is better suited for very small d_{PLA}. Especially the 30 µm PLA, which has an aSGT of virtually zero, is much easier to use with the Quanta 200 than with the Quanta 600. Figure 51 compares the FoV for the Quanta 200 and Quanta 600 as a function of d_{PLA} at an ED of 1.7 mm.
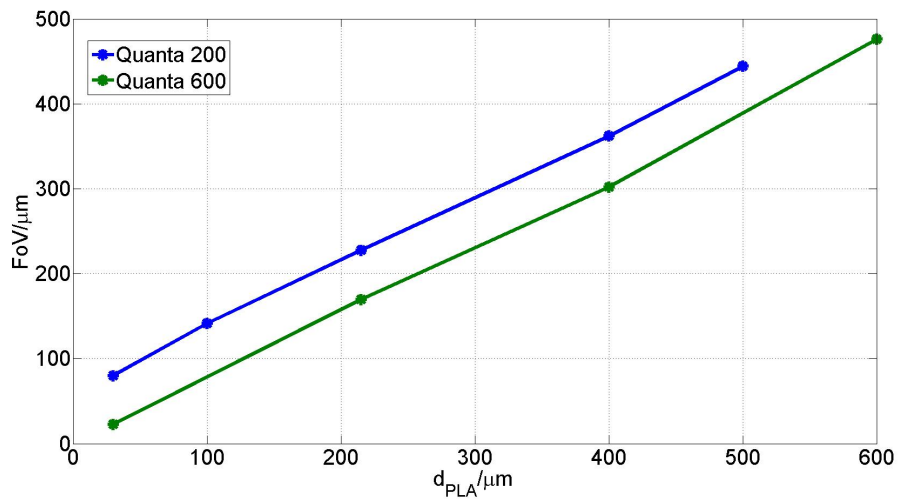
Figure 51: FoV of the Quanta 200 and Quanta 600 as a function of d_{PLA} at ED=1.7 mm.

45

## 5.2 Secondary electron detector

A new secondary electron detector was designed, that can be position any-where in the sample chamber and also allows for the usage of different electrode shapes. Putting the detector on the sample table, rather than the pole piece, makes the distance between the sample and the detector independent of the environmental distance. This allows for a strong amplification of the SE signal even at very small environmental distances. It also frees the place at the bottom of the pole piece, making it possible to use the backscattered electron detector. The image quality can also be improved by using a sharp electrode.

Unfortunately it is very difficult to directly compare the new experimental secondary electron detector (ESED) to the gaseous secondary electron detector (GSED) of FEI, using the SNR method described in chapter 4.1. For a straight forward comparison of the GSED and ESED it is necessary to choose the same ED for both detectors, but for the GSED the detector-sample distance is equal to the ED. As explained in chapter 5.2.2, a suitable detector-sample distance has to be chosen for a SE-detector to work to its full potential. One of the biggest advantages of the ESED is that the detector-sample distance is independent of the ED, which means that the ED can be made as small as possible without effecting the SE-amplification. The same is not true for the GSED, which when the sample is placed at a small ED might perform badly, because the detector-sample distance is too small. When a larger ED is used the biggest advantage of the ESED that it can perform well at smaller EDs than the GSED is nullified. Therefore using the SNR method an overall comparison of both the new detector and the new bullet to the original design is made in chapter 5.3.

5.2.1 Modifications

In order to use the FEI infrastructure and user interface a connector with the same pin setup as the original GSED was build. In this way it is possible to connect and use the ESED in the same way as the GSED without any further modifications. Figure 52 and 53 show the pin setup of the GSED. The pins 2 and 3 on the lower side and 3 and 4B on the upper side are connected to the suppressor electrode and pin 4 towards the chamber is connected to the detection electrode.
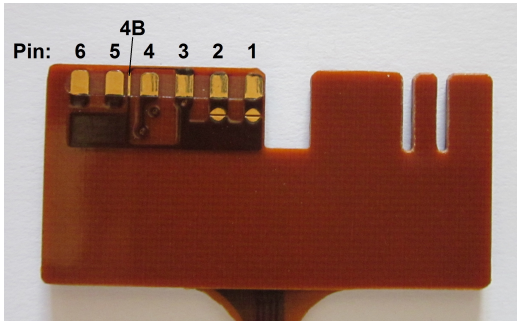
Figure 52: Pin setup of the GSED (lower side).
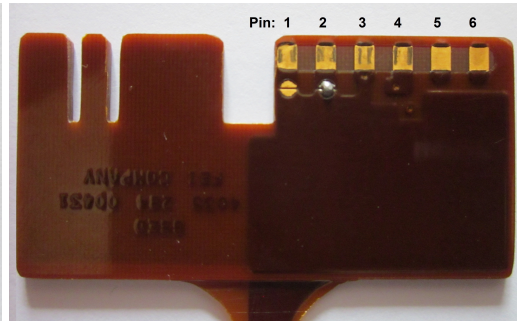
Figure 53: Pin setup of the GSED (upper side).

From the connector of the ESED a wire runs to the detection electrode. The electrode is interchangeable, because it is built in such a way that the wire can easily be disconnected from the electrode. The electrode can be placed anywhere in the sample chamber, but it is usually positioned on the sample table because then the distance between the sample and the detector is independent of the ED. Figure 54 shows a schematic drawing of the ESED.
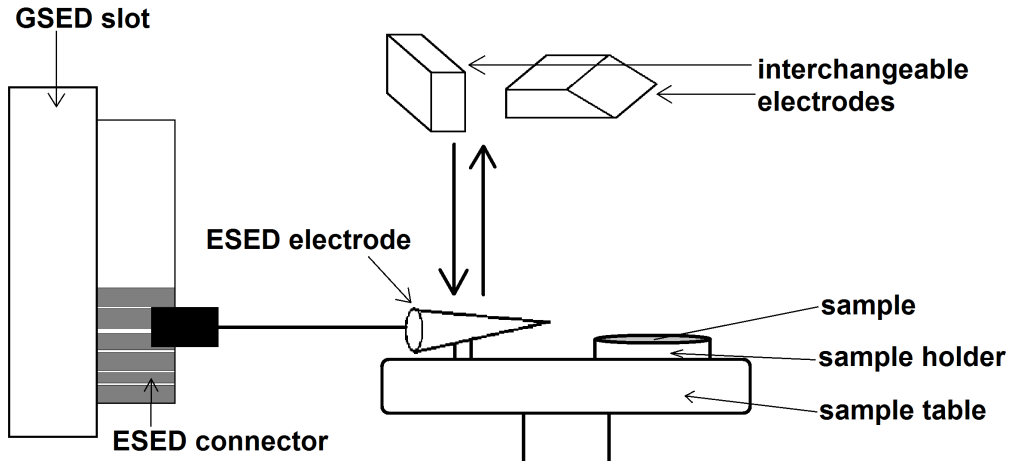
Figure 54: Schematic drawing of the ESED.

The main advantage of this design is that the distance between the sample and the detector is independent of the ED, which means that the gas amplification is independent of the environmental distance. This also helps to avoid arching at short environmental distances, which are required at high pressure. Another advantage is that different electrodes, namely sharp tips and edges, can be used in order to increase the gas amplification at high

pressures as proposed by [20]. Last but not least being able to choose the distance between the sample and the detector makes it possible to avoid both arching and reaching the maximum voltage that can be applied to the electrode.

5.2.2 Detector shape and position

Three different electrodes shapes were tested, a flat surface, a blade edge with an edge size of about 3 µm and a tip with a diameter of 0.5 µm. The GSED uses a flat electrode, a sharp tip has geometrical advantages and the blade is a mixed out of those two designs. Images of those three electrodes can be found in the appendix 8.5. The measurement was done using both water vapor and ambient air as imaging gas. The acceleration voltage was 30 kV, the ED was 6.7 mm for water vapor, the horizontal field width (HFW) was 10.67 µm, the diameter of the PLA 1 (d_{PLA}) was 200 µm and the sample-detector distance (d_{sd}) was 5 mm. Figure 55 shows the results for water vapor.
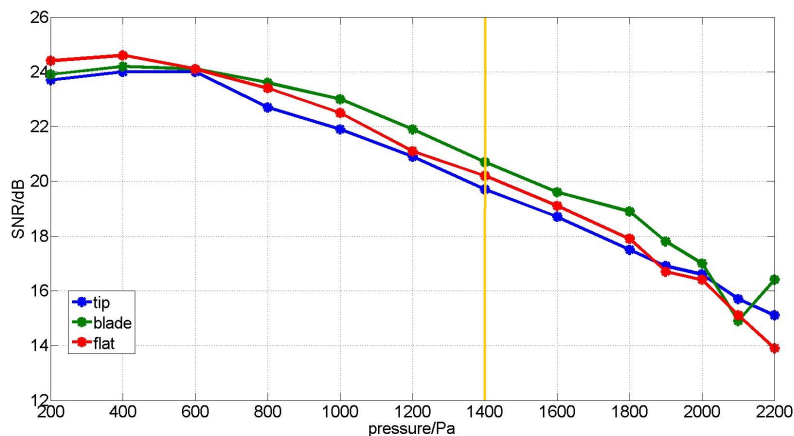
Figure 55: SNR as a function of pressure, using water vapor as imaging gas and a flat, tip and blade shaped electrode; the orange line marks the example images in figure 56-58.

The blade is the best design above 600 Pa. The flat electrode is the best design until 600 Pa and then remains the second best design until 1900 Pa, at which point the tip becomes the second best design. However, the difference best to worst is only approximately 1 dB for most pressures, which is not a lot given a measurement error of $\pm$ 0.4 dB, but since the blade is the best design for 10 out of 13 data points this still indicates an improvement over a

flat electrode. Figure 56-58 show the three images taken at 1400 Pa in figure 55.
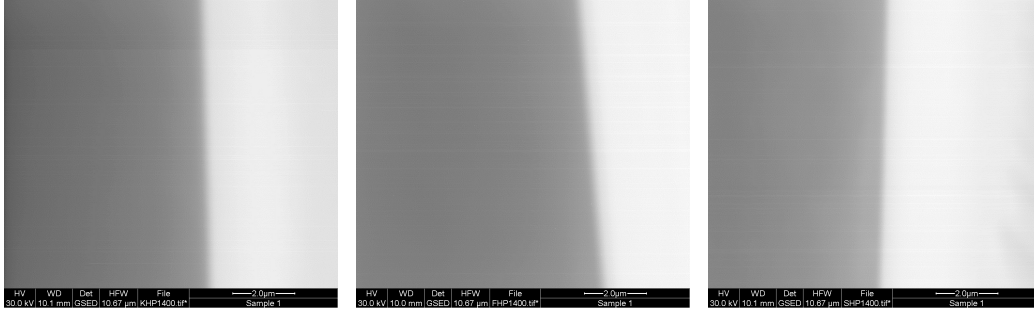
Figure 56: Image using the blade electrode at 1400 Pa; SNR: 20.7 dB.

Figure 57: Image using the flat electrode at 1400 Pa; SNR: 20.2 dB.

Figure 58: Image using the tip electrode at 1400 Pa; SNR: 19.7 dB.

Given the small difference of the SNR there is little visible difference. There is a slight, hardly visible difference of contrast between the best (blade) and the worst (tip) image. Figure 59 shows the achievable contrast measured in the measurement above.
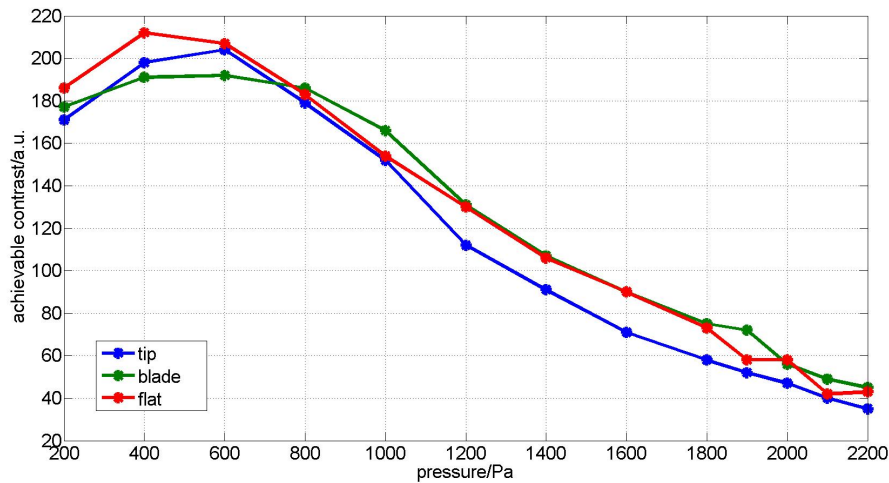

Figure 59: Achievable contrast as a function of pressure, using water vapor as imaging gas and a flat, tip and blade shaped electrode.

The contrast starts to decline above 600 Pa roughly following the same curve as the SNR. Figure 60 shows the estimated noise in the measurement above.
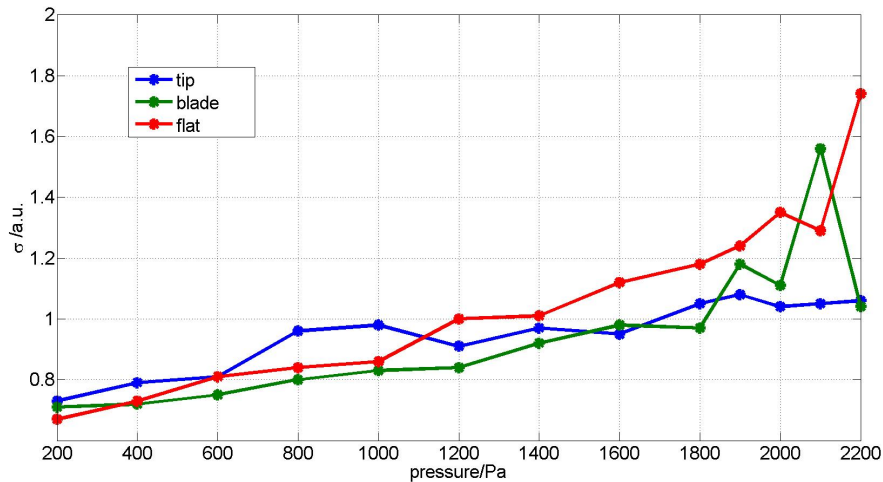

Figure 60: Estimated noise as a function of pressure, using water vapor as imaging gas and a flat, tip and blade shaped electrode.

With the exception of two outlier, the white noise is always between 0.7-1.4 a.u. and increases with increasing pressure. However, the noise is always small and is hard to notice in the image with the naked eye, whereas the loss of contrast is clearly visible. This is representative for all SNR measurements. The noise in general stays between 0.5-1.5 a.u. and the decrease in contrast is the main reasons for the decrease in SNR. The reason for noise values above 1.5 a.u. can be shifts in the beam current of the thermionic gun or a fluctuating gas pressure inside the chamber. In general noise values above 1.5 a.u. point to a cause of image quality loss unrelated to the secondary electron detector and are usually not reproducible.

The same measurement comparing the different detector shapes was also done using ambient air as imaging gas. The acceleration voltage was 30 kV, the ED was 4.7 mm for ambient air, the HFW was 10.67 µm, d_{PLA} was 200 µm and d_{sd} was 5 mm. Figure 61 shows the results for ambient air.
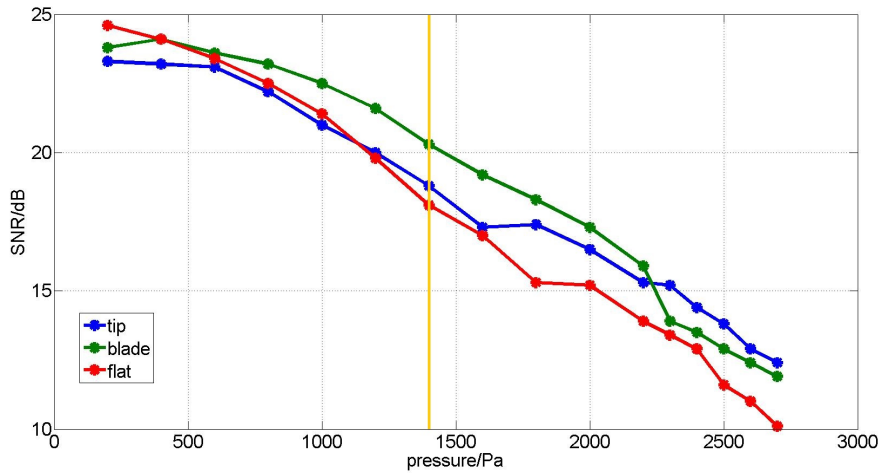
Figure 61: SNR as a function of pressure, using ambient air as imaging gas and a flat, tip and blade shaped electrode; the orange line marks the example images in figure 62-64.

The blade is again the best design between 600 and 2200 Pa, but the tip becomes the best design above 2200 Pa, whereas the flat electrode is the worst design above 1200 Pa. The difference best to worst is more significant than with water vapor. It is approximately 2 dB for most pressures. Both measurements indicate that an electrode shaped as a small tip or sharp blade is better than a flat electrode at high pressures. Figure 62-64 shows the three images taken at 1400 Pa in figure 61.
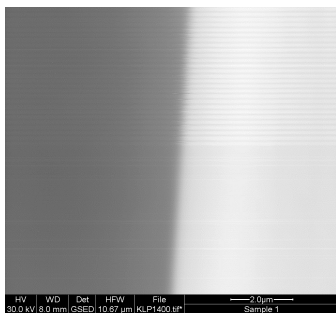

Figure 62: Image using the blade electrode at 1400 Pa; SNR: 20.3 dB.
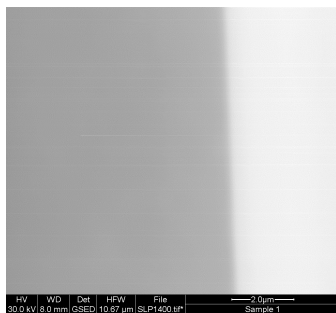
Figure 63: Image using the tip electrode at 1400 Pa; SNR: 18.8 dB.
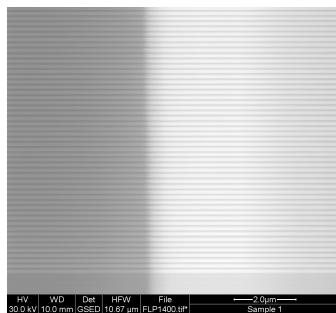
Figure 64: Image using the flat electrode at 1400 Pa; SNR: 18.1 dB.

51

The regular horizontal stripes in figure 64 and half of figure 62 are caused by an instable gas pressure inside the sample chamber that often occurs in the Quanta 200 ESEM at high pressures, when ambient air is used as an imaging gas. The SNR algorithm is designed in a way that it is not influenced by regular horizontal stripes. Compared to the other two electrodes, the blade has an advantage of 2.2 dB (area) and 1.5 dB (tip). The different contrast between the blade and the tip is clearly visible, whereas a difference of 1 dB in figure 56-58 was hardly visible, which puts the threshold for a visible improvement between 1-1.5 dB difference in SNR.

In order to investigate the influence of the tip size on the image quality, 5 different tip sizes (S) with diameters from 1 mm to 0.5 µm were tested at three different distances from the sample (d_{sd}= 1, 5, 10 mm). The acceleration voltage was 30 kV, the ED was 4.7 mm for ambient air and 6.7 mm for water vapor, the HFW was 10.67 µm and d_{PLA} was 200 µm. Figure 65 shows the results for water vapor and figure 69 shows the results for ambient air. Since the variation of d_{sd} made only very little and in order not to overload the figures, only the best result of the 0.5, 50, 500 µm diameter is displayed here. The full results can be found in the appendix 8.6.
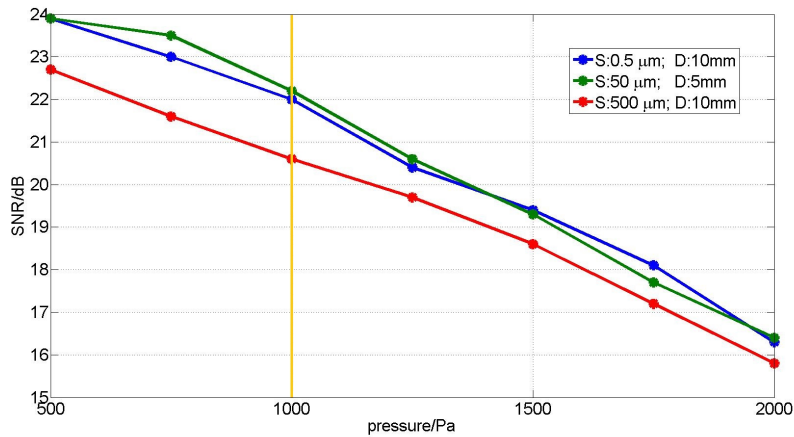
Figure 65: SNR as a function of pressure for different tip sizes (S) using water vapor as imaging gas; the orange line marks the example images in figure 66-68.

The results are similar to those in figure 55. The small tips (0.5 and 50 µm) are a little bit better than the 500 µm. However, the difference best to worst is only about 1-1.5 dB, which is the same as the threshold for a visible improvement. The major difference between this measurement and the

one in figure 55 is that the small tips are consistently better over the entire pressure range than the large one, which is very similar to the flat electrode. The results of the 0.5 mm tip are similar to those of the flat electrode at pressures higher than 1750 Pa, but about 1.5 dB worse at pressures below 1250. This means that at low pressures having a bigger detector area is an advantage. Figure 66-68 show the three images at 1000 Pa in figure. The improved contrast of the 0.5 and 50 µm tip over the 500 µm tip is clearly visible.
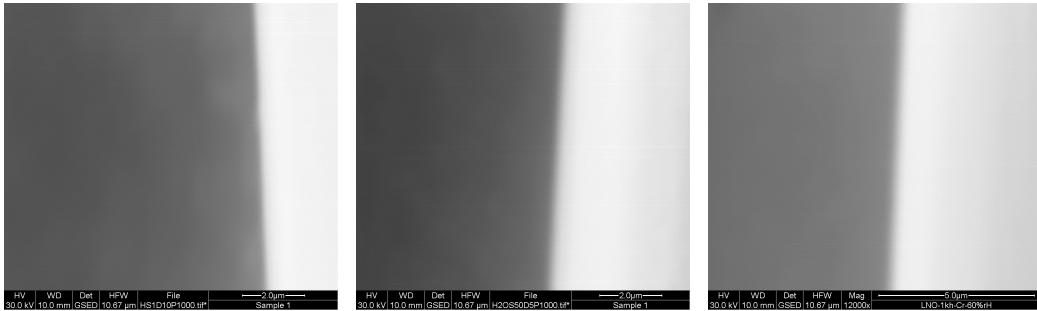
Figure 66: Image using the 0.5 µm tip at 1000 Pa; SNR: 22.0 dB.

Figure 67: Image using the 50 µm tip at 1000 Pa; SNR: 22.2 dB.

Figure 68: Image using the 500 µm tip at 1000 Pa; SNR: 20.6 dB.

Figure 69 shows the same measurements as figure 65 using ambient air as imaging gas and figure 70-72 show the three image at 1250 Pa in figure 69.
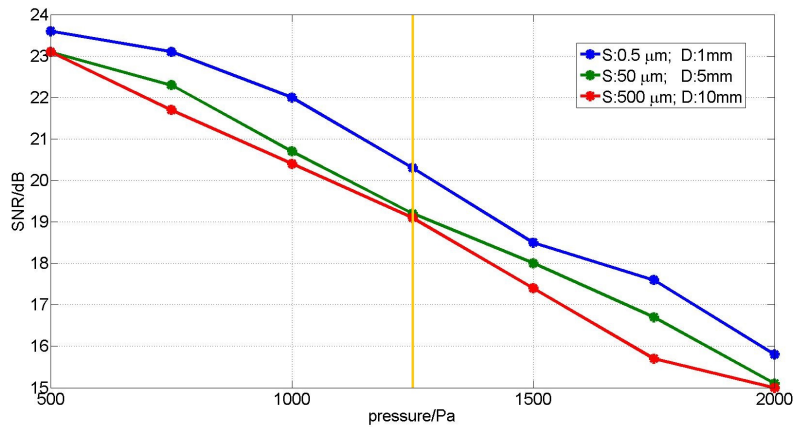

Figure 69: SNR as a function of pressure for different tip sizes (S) using ambient air as imaging gas; the orange line marks the example images in figure 70-72.
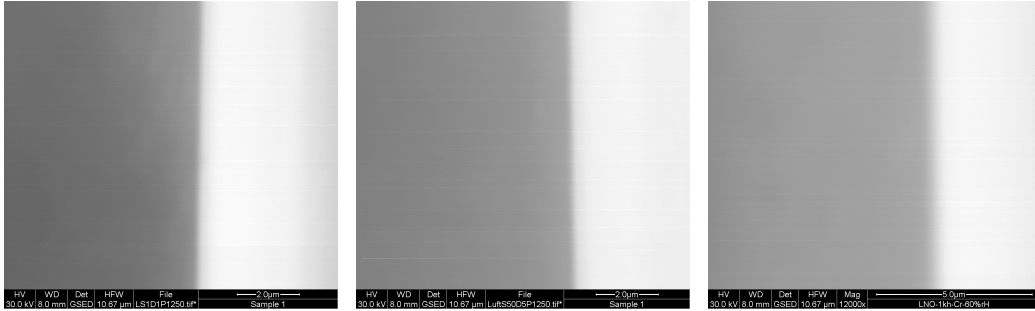
Figure 70: Image using the 0.5 µm tip at 1250 Pa; SNR: 20.3 dB.

Figure 71: Image using the 50 µm tip at 1250 Pa; SNR: 19.2 dB.

Figure 72: Image using the 500 µm tip at 1250 Pa; SNR: 19.1 dB.

The results using ambient air as imaging gas are similar to those using water vapor. The most significant difference is that the 50 µm tip is not much better than the 500 µm tip, whereas the 0.5 µm tip keeps an advantages of about 1-1.5 dB over all other tip sizes.

On one hand the tip size should be no more than a couple of µm, in order to take advantage of the benefits of a small tip size at high pressure for both imaging gasses water vapor and ambient air. On the other hand at low pressures having a bigger area provides an advantage. Therefore the blade is chosen as standard electrode shape. It has been proven to outperform the other electrode shape over a wide range of pressure ($\approx$ 600-2200 Pa) by combining the advantages of a small edge with those of a large area. This makes it suitable for most applications. However, for special application that require pressures above 2200 Pa a below 1 µm tip should be considered if the blade does not produce a sufficient image quality.

The effect of the detector-sample distance was further investigated by measuring the SNR as a function of d_{sd} at constant pressure. This was done using the blade electrode and ambient air as imaging gas. The acceleration voltage was 30 kV, the ED was 4.7 mm, the HFW was 10.67 µm and d_{PLA} was 200 µm. Two measurements were done at 1000 and 2000 Pa. Figure 73 show the results.
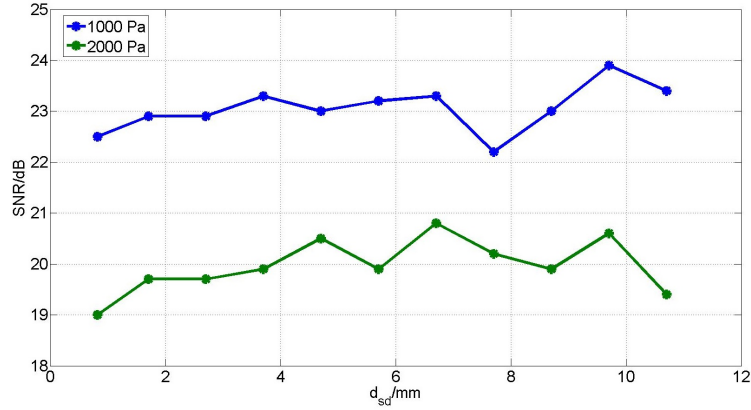
Figure 73: SNR as a function of d_{sd} for different pressures using ambient air as imaging gas.

It seems that the SNR increases with increasing d_{sd} but the standard deviation of both measurements is about 0.5 dB, which means that the increase is hardly significant given an estimated error of 0.4 dB. For a better understanding of these results figure 74 shows the voltage applied to the detector as a function of d_{sd}. The voltage is linearly dependent on the contrast setting of the microscope. The voltage is therefore simply measure by recording the contrast settings of the microscope. The voltage(U) can be calculated form the contrast setting(C) with the formula provided by Rattenberger [21]:

$$U = -0.34 + 5.18 * C \tag{21}$$
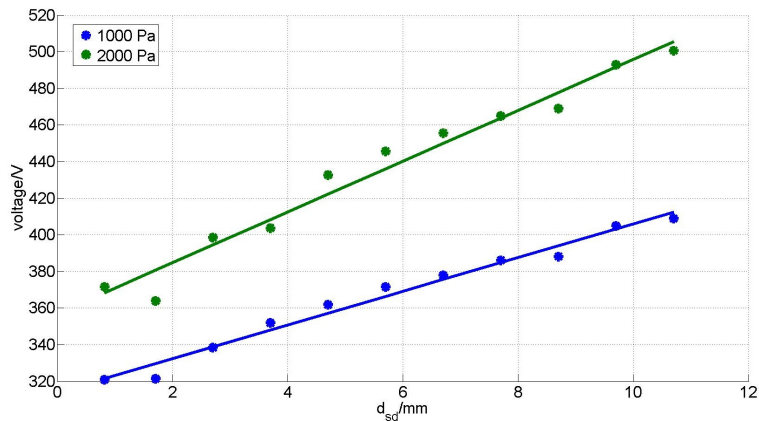
Figure 74: Voltage applied to the electrode of the ESED as a function of d_{sd}.

55

There is a linear relation between d_{sd} and the voltage applied to the electrode (U). The average electric field strength ($\overline{\chi}$) is given by:

$$U = \overline{\chi} * d_{sd} \qquad (22)$$

This means that the average electric field strength remains the same if d_{sd} is changed, because the voltage changes accordingly. According to the SNR measurement in figure 73 the SNR stays the same, when d_{sd} is varied as long as it is possible to keep the average electric field strength constant by changing the voltage. This is impossible if d_{sd} become very large, because the voltage required to do so is above the maximum voltage that can be applied. Another reason why increasing the detector voltage becomes impossible is arching, which occurs very often at high detector bias.

To summarize, in order to achieve optimal conditions, the detector can be positioned anywhere as long as there is no arching and the maximum voltage applicable to the detector is not reached. From a practical point of view it is unreasonable to put the detector at less than 1 mm away from the sample. Also the ESEM is often used to investigate large areas and putting the detector very close to the sample would make d_{sd} dependent on the scanning pattern at small magnifications.

5.2.3 SNR dependence on pressure and scattering

The blade design was further investigate by measuring the SNR as a function of pressure for a constant average number of scattering events per electron (m). This is done by calculating the ED necessary to achieve the desired average number of scattering events per electron for any given pressure using formula 2 and the results from chapter 5.1.3. The measurements were performed using both ambient air and water vapor as imaging gas. The acceleration voltage was 30 kV, the HFW was 10.67 µm, d_{PLA} was 215 µm, m was 1.5 and d_{sd} was 5 mm. Figure 75 shows the EDs used and figure 76 shows the results.
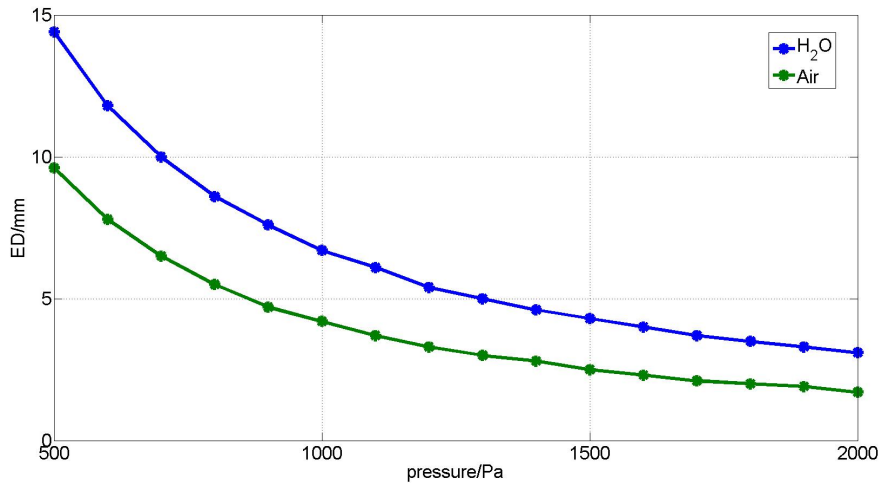
Figure 75: EDs used in order to achieve m=1.5 for different pressures.
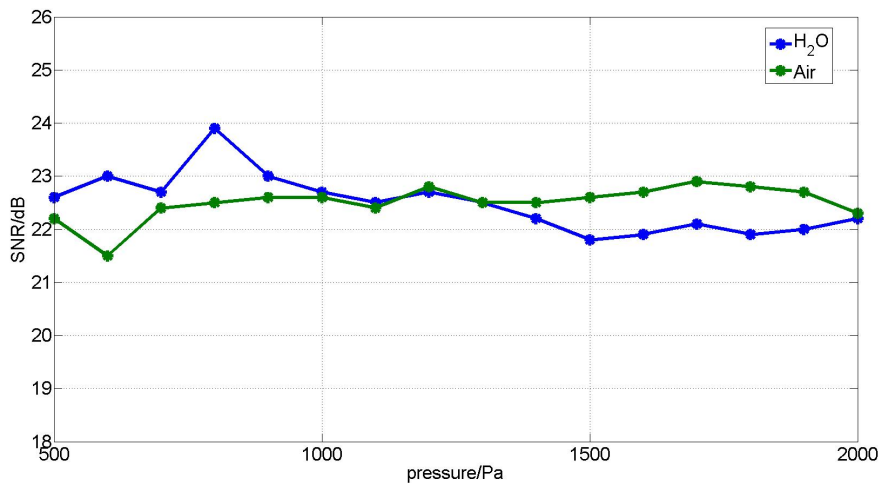
Figure 76: SNR as a function of pressure for different imaging gasses and m=1.5.

There is no significant influence of the pressure on the SNR as long as the average number of scattering events is kept constant. By using water vapor the SNR is slightly decreasing at high pressures due to an increase of white noise, the effect is however barely measurable. The standard deviation of the water vapor measurements is 0.54 dB, compared to an estimated error of ± 0.4 dB of the measurement technique. In comparison to water vapor the results for ambient air as imaging gas do not show this decrease. Furthermore

the SNR is not influenced by the imaging gas, as long as the average number of scattering events is kept constant. The average SNR value of water vapor is 22.48 dB and that of ambient air 22.5 dB. Figure 77 shows the voltage applied to the detector in the measurement in figure 76. It was determined in the same way as in chapter 5.2.2.
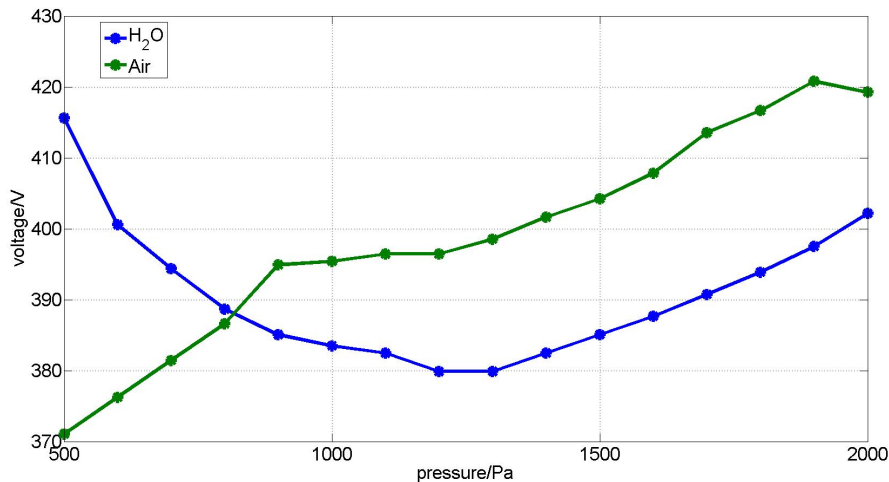
Figure 77: Voltage applied to the ESED as a function of pressure.

The voltage increases for ambient air as the pressure increases. For water vapor there is a minimum at about 1250 Pa and the voltage increases above 1250 Pa as pressure increases. Equation 8 shows that in order to hold the Townsend's first ionization coefficient the voltage has to change as:

$$U = \frac{C_1 * P}{ln(C_2 * P)} \tag{23}$$

where C_1 and C_2 are constants depending on the free mean path of inelastic scattering of an electron at the unit pressure and the ionization energy of the gas.

Both graphs follow a function of this shape were the minimum of the ambient air graph is below 500 Pa. Water vapor requires less voltage above 800 Pa than ambient air, which means that water vapor is a better imaging gas at high pressure. However, the results in figure 76 show that as long as the voltage can be adjusted (U_{max} = 518 V) the same image quality can be achieved with both gases at all pressures.

The influence of scattering was investigated by measuring the SNR as a function of the average number of scattering events per electron. This is done

by choosing a constant pressure and then calculating the ED necessary to achieve the desired average number of collision per electron. The measurement was performed using both ambient air and water vapor as imaging gas. The acceleration voltage was 30 kV, the HFW was 10.67 µm, d_{PLA} was 215 µm, d_{sd} was 5 mm and the pressures used were 1000 and 2000 Pa. Figure 78 shows the results.
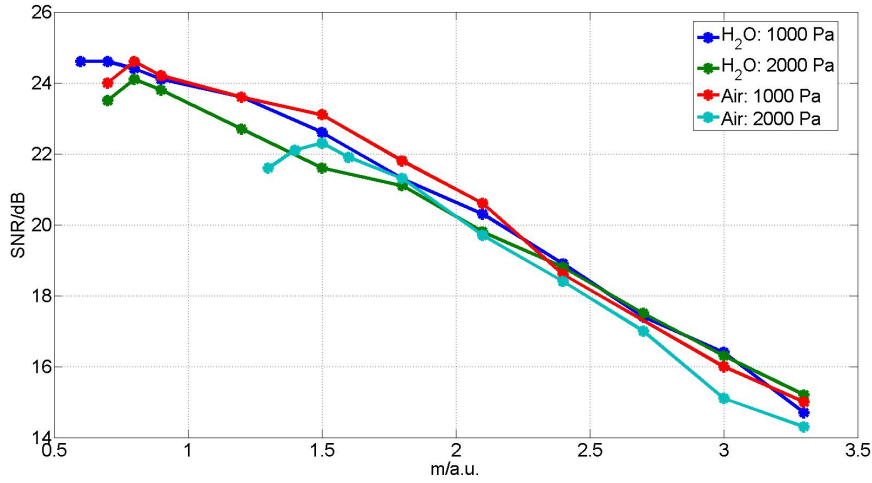
Figure 78: SNR as a function of m for different pressures and imaging gas.

There are again no significant differences caused by the pressure or imaging gas. There is a linear relation between m and the SNR. As explained in chapter 5.2.2, the decrease of SNR is driven mostly by a decrease of contrast. For this reason the SNR is approximately a logarithmic representation of the contrast. The contrast itself depends on the detector setup and the ratio of scattered to unscattered electrons, as explained in chapter 3.2, and m is a logarithmic representation of that ratio:

$$SNR = 10 * log_{10}(\frac{Signal}{Noise}) \overset{Noise \approx cons.}{\propto} ln(Signal) \propto ln(\frac{I}{I_0}) = m \qquad (24)$$

$$==> SNR \approx C_{detector} * m + d_{detector} \qquad (25)$$

m is given by the beam transfer characteristics discussed in chapter 5.1. $C_{detector}$ and $d_{detector}$ are constants that summarize the overall quality of the SE-detector. They are determined by taking the average of the 4 measurements in figure 78. The data points below m=1 are ignored because the signal, being measured in the gray value scale of the image, cannot be bigger

than the highest possible difference in gray value of 256. Figure 79 shows the average of the 4 measurements in figure 78 above m=1 and the linear fit used to determine C_{blade} and d_{blade}.
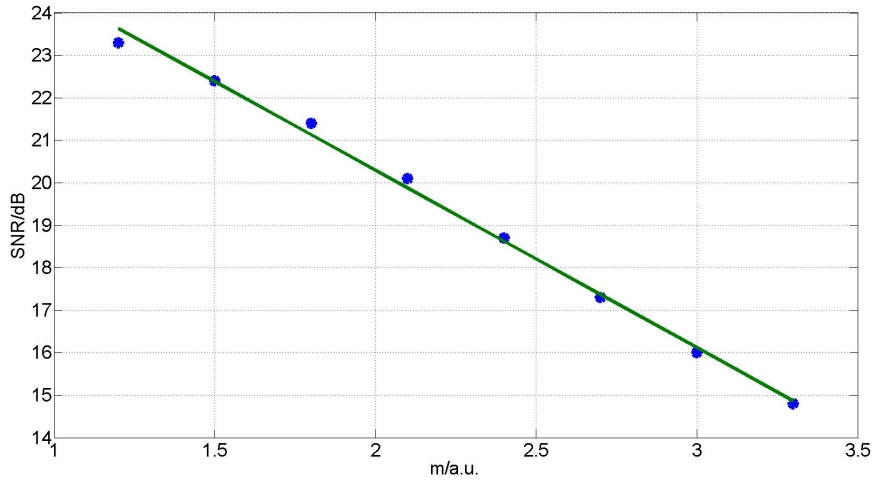
Figure 79: SNR as a function of m for the blade design with linear regression.

The Fit parameters of the linear regression are:

$C_{blade} = -4.2 \frac{dB}{a.u.}$
$d_{blade} = 28.6 \ dB$

Keeping in mind that, due to the limit of the signal imposed by the gray value scale, the SNR is approximately limited to 24 dB. The SNR of the blade detector is therefore approximately given by:

$$SNR[dB] \approx \begin{cases} -4.2 * m + 28.6 & \text{if } -4.2 * m + 28.6 \leq 24 \\ 24 & \text{if } -4.2 * m + 28.6 \geq 24 \end{cases} \qquad (26)$$

The results in figure 55 and 61 can be used to determine the SNR as a function of m for the sharp tip and flat electrode. This was done by calculating m for every data point in figure 55 and 61 and calculating the arithmetic mean. Figure 80 show the SNR as a function of m for the sharp tip, flat and blade electrode.
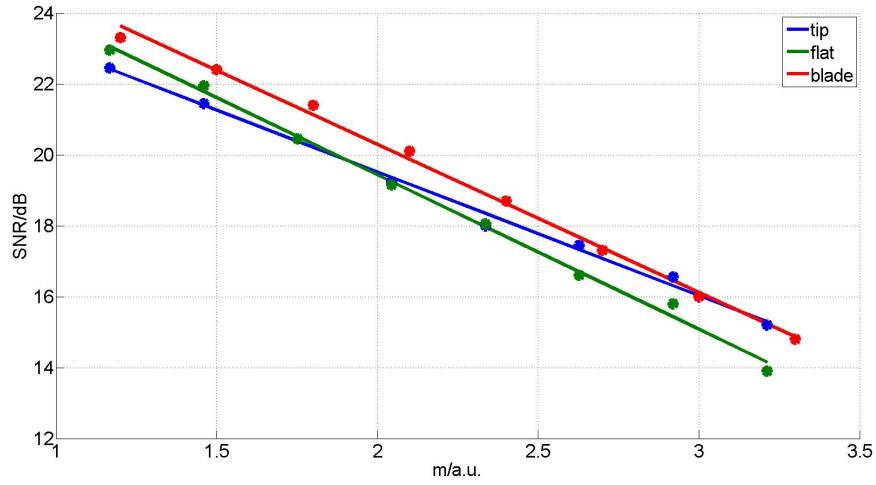
Figure 80: SNR as a function of m for the sharp tip, flat and blade electrode.

The Fit parameters are:

$C_{tip} = -3.5 \; \frac{dB}{a.u.}$
$d_{tip} = 26.5 \; dB$
$C_{flat} = -4.4 \; \frac{dB}{a.u.}$
$d_{flat} = 28.1 \; dB$
$C_{blade} = -4.2 \; \frac{dB}{a.u.}$
$d_{blade} = 28.6 \; dB$

This means that the blade electrode always outperforms the flat electrode. The sharp tip is better when there is a lot of scattering and worse when there is few scattering than the other two. The blade detector has to be preferred, because the sharp tip becomes better than it at a SNR that is already unsuitable for imaging.

5.3   Overall improvements

Two modifications have been made to improve the image quality in high pressure SEM. The more efficient and variable design of the bullet, described in chapter 5.1, reduced the scattering of the electron beam and the new SE-detector, described in chapter 5.2, improves the efficiency of the SE-detection. Choosing a different electrode shape and putting the detector on the sample table rather than on the pole piece clearly improves image quality. The sample-detector distance is now independent of the ED and the position at the end of the pole piece is free to use the SE and BSE detector (SSD) simultaneously.

The overall improvement achieved by those two modifications is measured using the SNR method described in chapter 4.1. and compared with the original design. As explained in chapter 5.2, comparing the new design to the original at a fixed ED is not very useful. The comparison is therefore made by choosing the best possible ED at any given pressure for both designs. The best possible ED for the new design is simply the shortest possible ED, whereas the best possible ED of the original design has to be chosen experimentally. The drawback of this method is that this introduces a new source of error. The advantage is that it is similar to how an ESEM is used in practice. Figure 81 shows the results of this measurement using water vapor. The acceleration voltage was 10 kV, the HFW was 10.67 µm, d_{PLA} was 215 µm (for the SSD and ESED with the blade electrode), d_{sd} was 1 mm and the EDs used are given in table 1 in the appendix 8.7.
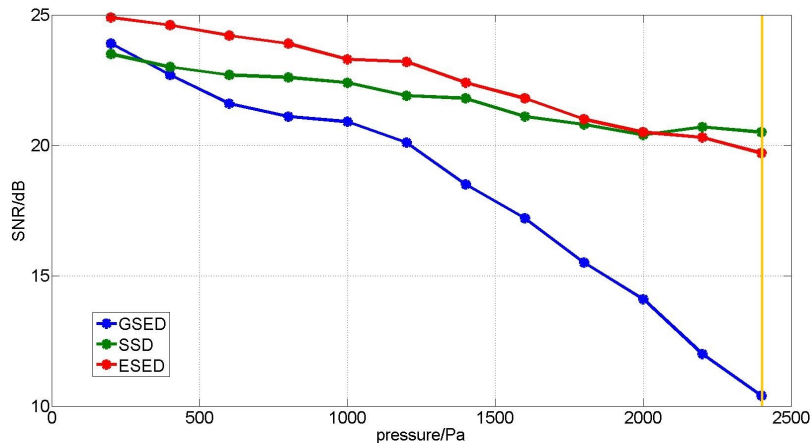

Figure 81: Comparing the original design (GSED), to the new one (SSD and ESED) under practical working conditions using water vapor; the orange line marks the example images in figure 82-84.

The image quality using the new design is high over the entire range of the measurement, whereas the image quality using the GSED rapidly decreases above 1200 Pa and becomes unsuitable for imaging at about 2000 Pa. Figure 82-84 show the pictures taken at 2000 Pa.
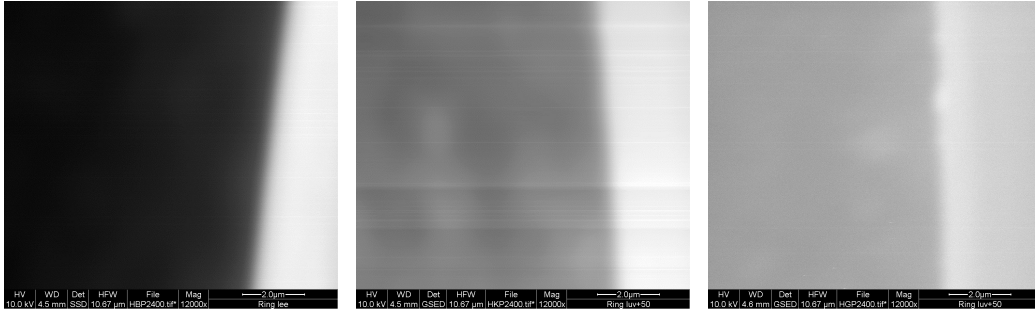
Figure 82: Image using the SSD at 2400 Pa; SNR: 20.4 dB.

Figure 83: Image using the ESED at 2400 Pa; SNR: 19.8 dB.

Figure 84: Image using the GSED at 2400 Pa; SNR: 10.5 dB.

The ED for the SSD and ESED is 1.2 mm and for the GSED is 0.1 mm. Unfortunately, the advantage of the new bullet is divided in half because of the software restrictions of the microscope (see chapter 5.1.3). The difference in contrast between the ESED and GSED is not as big as expected form the difference in SNR, because a very short ED was chosen for the GSED. However, this short amplification distance towards the detector increases the noise in the GSED images dramatically[22]. In the images shown below the contrast for the GSED is 45 a.u. and the noise is 4.1 a.u. compared to a contrast of 108 a.u. and a noise of 1.1 a.u. for the ESED. Above 1400 Pa the ED was kept as short as possible because even at the same SNR, a loss of contrast is much worse than an increase in noise for image quality. This is also the explanation for the GSED image looking not as much worse than the ESED image as indicated by the SNR difference. The horizontal stripes in the ESED image are caused by a fluctuating gas pressure, but these image artifacts do not influence the image analysis.
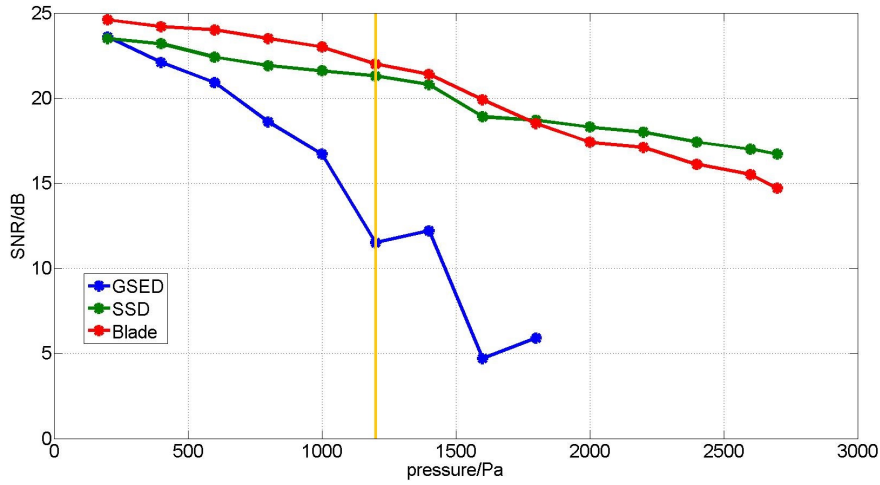
Figure 85: Comparing the original design (GSED), to the new one (SSD and ESED) under practical working conditions using ambient air; the orange line marks the example images in figure 86-88.

Figure 85 shows the same measurement as figure 81 using ambient air as imaging gas. The new design maintains high image quality until about 1500 Pa and acceptable image quality over the entire pressure range. Because of the higher scattering cross-section of ambient air compared to water vapor, the advantages of the shorter stagnation gas thickness of the new bullet are much more relevant. The GSED quickly loses image quality above 600 Pa and images above 1200 Pa are unacceptable. Figure 86-88 show the pictures taken at 1400 Pa.
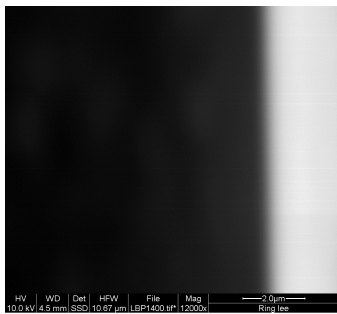

Figure 86: Image using the SSD at 1400 Pa; SNR: 20.8 dB.
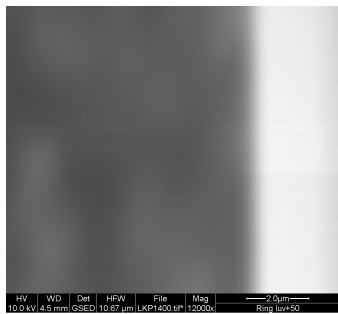
Figure 87: Image using the ESED at 1400 Pa; SNR: 21.4 dB.
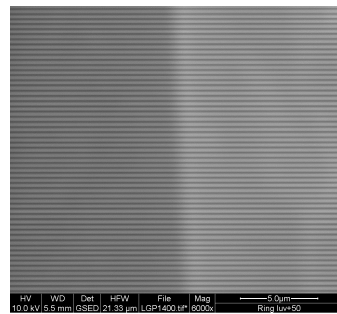
Figure 88: Image using the GSED at 1400 Pa; SNR: 12.2 dB.

64

A strong loss of contrast and regular horizontal stripes are visible in the GSED image. These regular horizontal stripes are again caused by a fluctuation of gas pressure inside the sample chamber that often occurs in the Quanta 200 ESEM at high pressures when ambient air is used as imaging gas. The loss of contrast compared to the ESED and SSD images is significant. Furthermore it was impossible to make the ED smaller than 1 mm for the GSED because the image was either completely black or white. Therefore the new bullet kept almost its full aSGT advantage in these images and a similar difference in contrast can be expected using water vapor as imaging gas, if the software limitations mention in chapter 5.1.3 could be lifted.

In order to demonstrate the improvements figure 89-91 show images of gold particles on a carbon substrate taken with the new and original design at the Quanta 600 microscope, which has a higher resolution than the Quanta 200. The images were taken at 2.2kPa (water vapor) and 2.7 kPa (ambient air) using an acceleration voltage of 10 kV and a WD of 5.8 mm.
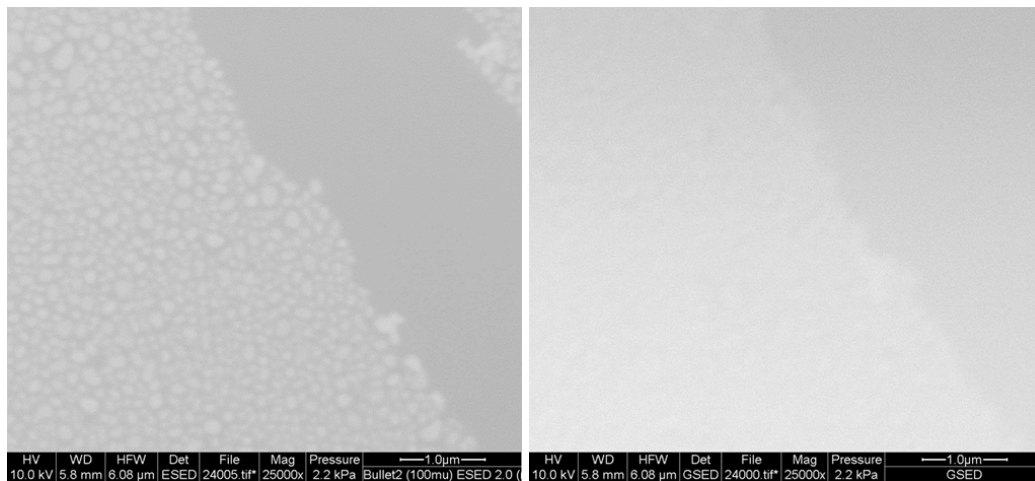
Figure 89: Gold particles on carbon using the ESED and water vapor.

Figure 90: Gold particles on carbon using the GSED and water vapor.
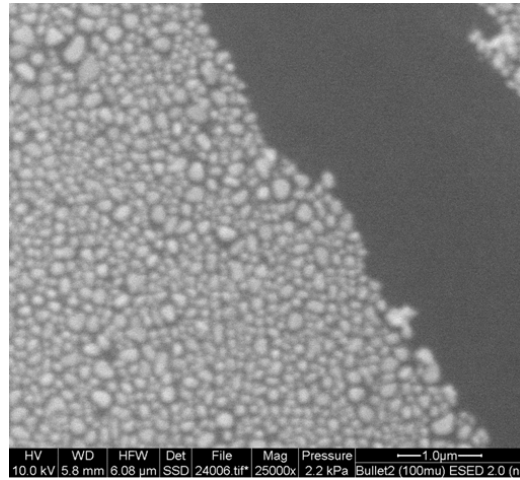
Figure 91: Gold particles on carbon using the SSD and water vapor.

The ESED still produces a useful image, whereas there is hardly anything visible in the GSED image. The backscatter image still has a similar quality as in high vacuum. The resolution remains the same as in high vacuum as long as there is sufficient contrast. Even the smallest gold particles are clearly visible in the SSD image and most of them are also visible in the ESED image. Figure 92 and 93 show the same part of the sample using ambient air at 2.7 kPa.
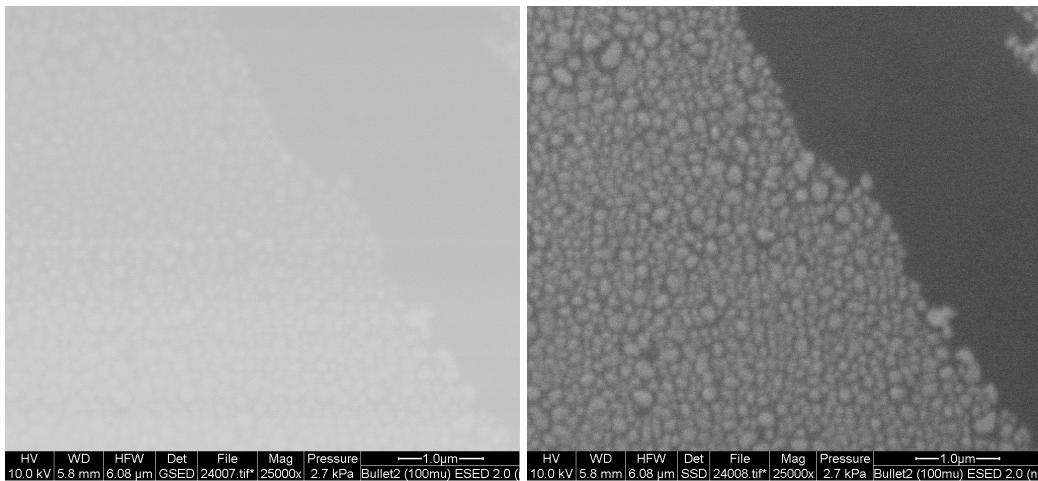
Figure 92: Gold particles on carbon using the ESED and ambient air.

Figure 93: Gold particles on carbon using the SSD and ambient air.

It was impossible to take an image using the GSED at 2.7 kPa with ambient air as imaging gas, whereas the results using the new designs are similar to those using water vapor. A small loss of contrast compared to the image using water vapor is visible in the SSD image. The ESED image has considerably less contrast than the image using water vapor, due to the more difficult imaging condition. However, the big gold particles are still visible and the image would still be useable if enhanced digitally, as is demonstrated in figure 94.
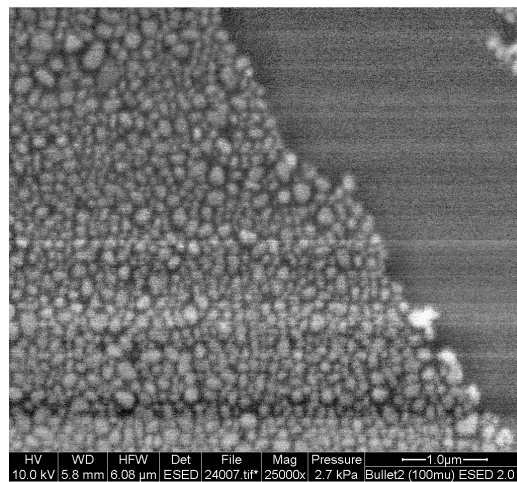
Figure 94: Image in figure 92 with digitally enhanced contrast.

By experience and interpreting images with different SNR in chapter 5.2, 5.3 and appendix 8.3 the threshold for the highest image quality possible is 22 dB and the threshold for useable imaging is around 15 dB depending on the source of the decrease in SNR. By using equation 26 in chapter 5.2.3 the SNR using the ESED with the blade electrode can be calculated as a function of m. m can be calculated using equation 2 in chapter 3.2, the additional SGT is provided in chapter 5.1.3, and the total scattering cross-section is provided by Rattenberger [19] for any given ED, acceleration voltage and pressure.
Combining all these information we can estimate the limits of the new design. Figure 95 shows the lines for SNR=22 dB and SNR=15 dB as a function of pressure and acceleration voltage, assuming the closest ED currently possible of 1.2 mm and a constant additional SGT of 0.5 mm for water and 1 mm for ambient air, using a 215 µm PLA.
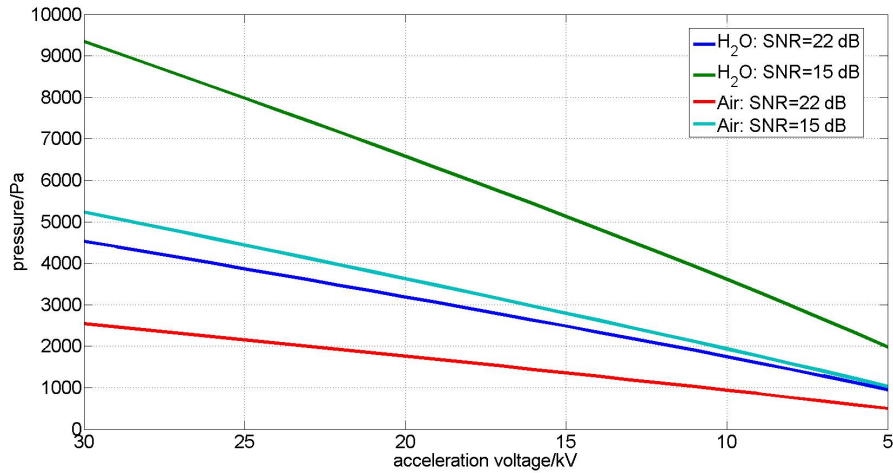
Figure 95: Estimation of the limits of the new design at ED=1.2 mm.

Compared to the measurements in figure 81 and 85, the estimation is correct for water vapor, whereas the limits for air are slightly underestimated. The maximum pressure that can be set on the Quanta 200 is 2700 Pa. According to this estimation it is possible to get highest quality images using water vapor and an acceleration voltage of more than 15 kV as well as acceptable image quality using an acceleration voltage of more than 7 kV over the entire pressure range. By using air as imaging gas an acceleration voltage of 30 kV is required to achieve the highest possible quality and an acceleration voltage of more than 15 kV to achieve acceptable image quality over the entire pressure range. By using high acceleration voltages it should also be possible to achieve good image quality even at pressures well beyond the current 2700 Pa limitation of the microscope.

However, this simulation does not represent the theoretical limit of what is possible using the new design. Unfortunately, the ED is limited to be bigger than 1.2 mm by the software of the ESEM, which makes it impossible to reach the full potential of the new design. If it were possible to lift this limitation, the sample could easily be placed at an ED of at least 0.3 mm. Figure 96 shows an estimation of the limits of the new design using the same parameters as the estimation in figure 95 but an ED of 0.3 mm.
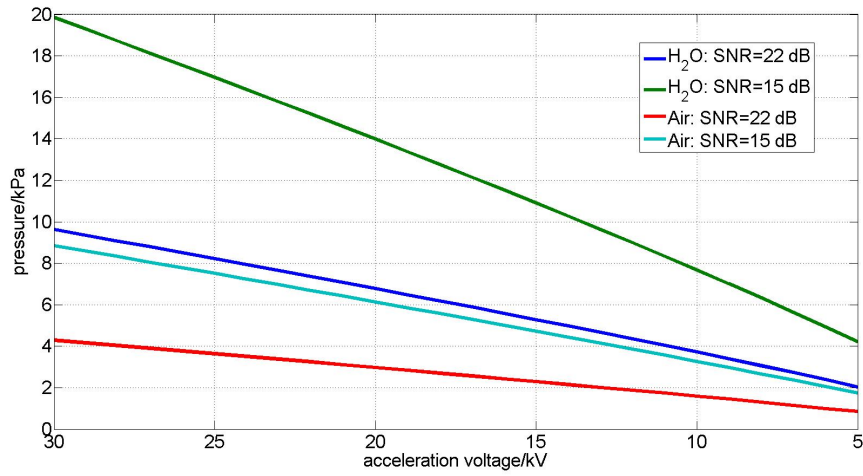
Figure 96: Estimation of the limits of the new design at ED=0.3 mm.

In this case highest quality above 18 kV using air and 7 kV using water vapor should be possible. Acceptable image quality is possible above 5 kV using water vapor and be possible above 9 kV using air. Pressure ranges way beyond the current 2700 Pa limit of the microscope should be possible assuming that the column is still sufficiently protected, which is indicated by the pressure measurements in chapter 5.1.2.

6 Conclusion

Previous works suggest that improvements of the beam transfer and the secondary electron detection in an environmental scanning electron microscope are possible. This work concentrates on implementing modifications to the pressure limiting system and the SE-detector and investigating the effects of those modifications on the image quality.

The beam transfer characteristics can be tremendously improved by optimizing the gas flow dynamics of the pressure limiting system. The additional stagnation gas thickness above the PLA 1 was reduced by 1.2 mm for water vapor and 2 mm for air by changing the shape of the bullet and the thickness of the PLA 1. The aSGT was further improved by reducing the diameter of the PLA 1. The smallest aSGT was achieved using a 30 µm PLA 1. It was 3 mm for water vapor and 4.25 mm for ambient air shorter than in the original design. However, using a very small PLA 1 strongly reduces the field of view. Therefore, the best compromise between FoV and aSGT was achieved using a 215 µm PLA 1, which reduces the aSGT by 2.5 mm for water vapor and 3 mm for air. Further research would be desirable regarding the effects of the interior shape of the bullet and the length of the bullet on the beam transfer. Also the possibility of customizing the bullet for a given experimental setup should be explored given the relatively low costs and the potential gains in image quality and pressure range.

In order to investigate the modifications of the SE-detector a matlab script was written which calculates the SNR and achievable contrast of a single SEM picture of a standardized sample. The two significant improvements in SE-detection are concerning the shape and the position of the detector. By using the newly developed SNR-method it can be shown that changing the shape to a needle or blade rather than an area detector yields a small improvement at high pressures. Positioning the electrode on the sample table rather than the pole piece makes the sample-detector distance independent of the environmental distance. This makes it significantly easier to operate at small EDs which are necessary at high pressures and it also allows the simultaneous use of the SE- and BSE-detector. The influence of the detector-sample distance was investigated. It was found that the image quality is independent of the sample-detector distance as long as the voltage applied to the detector does not reach its maximum value, there is no arching and the sample-detector distance is at least 1 mm. If all of these three conditions are met, the image quality is also independent of the chamber pressure as long as the ED is adjusted in a way that the total amount of beam scattering remains constant. This means by positioning the sample in a correct way the image quality is

only dependent on the average number of scattering events per electron (m) for any given electrode shape. A linear relation between m and the SNR was found for the proposed new detector design, which makes it possible to fully characterize the detector setup. It would be desirable to further investigate other detector setups in this way and also to do a detail computer simulation of the amplification taking place in the imaging gas. This might reveal possibilities to further improve SE-detection.

Finally it is shown that the combination of the improvements of the beam transfer characteristics and the detector setup yields a significant improve of image quality above 500 Pa. Especially maintaining high image quality above 2000 Pa using water vapor and a relatively low acceleration voltage of 10 kV. An estimate of the limitations of the new design predicts that imaging beyond 10 kPa should be possible. The possibility of SEM imaging in excess of 10 kPa on slightly modified commercially available ESEMs should be the topic of further research.

7 Literature

1. Danilatos G.D., Implications of the figure of merit in environmental SEM, *Micron, Vol. 44, p. 143-149*, 2013.

2. Danilatos G.D. et al., Matthew P.R., Nailon J.V., Electron beam loss in commercial ESEM, 16th *Australian conference on electron microscopy, Canberra, abstracts: 81-82*, 2000.

3. Danilatos G.D., Rattenberger J., Dracopoulos V., Beam transfer characteristics of a commercial environmental SEM and a low vacuum SEM, *Journal of Microscopy, Vol. 242, p. 166-180*, 2011.

4. Danilatos G.D., Optimum beam transfer in the environmental scanning electron microscope, *Journal of Microscopy, Vol. 234, p. 26-37*, 2008.

5. Rattenberger J., Improved understanding of scattering processes and their meaning for quantitative image interpretation in advanced scanning electron microscopy, *Ph.D. thesis at Graz University of Technology, Austria*, 2010.

6. Danilatos G.D., Electron scattering cross-section measurements in ESEM, *Micron, Vol. 45, p. 1-16*, 2013.

7. Thiel B.L., Bache I.C., Fletcher A.L., Meredith P., Donald A.M., An improved model for gaseous amplification in the environmental SEM, *Journal of Microscopy, Vol. 187, p.143-157*, 1997.

8. Johnson R., Environmental scanning electron microscopy; An introduction to ESEM®, *Philips Electron Optics brochure, Eindhoven*, 1996.

9. Danilatos G.D., Foundations of environmental scanning electron microscopy, *Advances in Electronics and Electron Physics, Vol. 71, p. 109-250*, 1988.

10. Danilatos G.D., Equations of charge distribution in the environmental scanning electron microscope, *Scanning Microscopy, Vol. 4, No. 4, p. 799-823*, 1990.

11. Dracopoulos V. et Danilatos G.D., ESEM modifications to LEO SUPRA 35 VP FESEM, *Micron, Vol. 44, p. 238-245*, 2013.

12. Goldstein J.I., Newbury D.E., Joy D.C., Lyman C.E., Echlin P., E Llfshin E., Sawyer L., Michael J.R., Scanning electron microscopy and X-ray microanalysis, 2nd Edition, *Plenum Press, New York*, 1992.

13. Knowles W.R., Toth M., Thiel B.L., Schroemges R., Ion control for optimized imaging with a novel gaseous detector, *Microscopy and Microanalyses 11, p. 28-29*, 2005.

14. Morgen S.W., Gaseous secondary electron detection and cascade amplification in the environmental scanning electron microscope, *Ph.D. thesis at the Sydney University of Technology, Australia*, 2005.

15. Thiel B.L., Tileli V., Low voltage and low vacuum - when worlds collide, *Microscopy and Microanalysis 12, p. 1436*, 2006.

16. Thiel B.L., Master curves for gas amplification in low vacuum and environmental scanning electron microscopy, *Ultramicroscopy, Vol. 99, Issue 1, p.35.-47*, 2004.

17. Meredith P., Donald A.M., Thiel B.L., Electron-gas interactions in the environmental scanning electron microscopes gaseous detector, *Scanning, Vol. 18, p. 467-473*, 1996.

18. Alparone L., Selva M., Aiazzi B., Baronti S., Butera F., Chiarantini L., Signal-dependent noise modeling and estimation in new generation imaging spectrometers, *Proc. 1st Workshop Hyperspectral Image Signal Process.:Evol. Remote Sens., p.1-4*, 2009.

19. Rattenberger J., Wagner J., Schröttner H., Mitsche S., Zankel A., A method to measure the total scattering cross section and effective beam gas path length in a low-vacuum SEM, *Scanning, Vol. 31, p. 107-113*, 2009.

20. Toth M., Uncovsky M., Kowles W.R., Baker F.S., Secondary electron imaging at gas pressures in excess of 1 kPa, *Applied Physics Letters, Vol. 91, p. 053122 - 053122-3*, 2007.

21. Rattenberger J., Advanced investigations of electron-gas interaction in an ESEM used for contrast formation, *Diploma Thesis at Graz University of Technology, Austria*, 2006.

22. Tileli V., Thiel B.L., Modeling noise in gas cascade secondary electron amplifiers, *Microscopy and Microanalyses 12, p. 1482-1483*, 2006.

8 Appendix

8.1 Source code of the SNR-script

This matlab script loads the pictures, cuts the databars out of them, defines a ROI and allows the processing of several pictures at once. The actual calculating of the SNR is done by the function SNRMedian2, which is the next script after this one.

```matlab
1  clear all
2  close all
3  clc
4  tic
5  %%%%%%%%%%%%%%%%Load pictures%%%%%%%%%%%%%%%%%%%%%%%
6  %The number of pictures to be investigate has to be provided
7  numberofpictures=1;
8  %This creates a Matrix in which all pictures will be stored
9  M=zeros([884,1024,numberofpictures]);
10 %Loads the picture by putting the directory of the picture ...
       where it says directory of picture
11 M2=imread('Directory of picture');
12 %This cuts the data bar out of a standard resolution ...
       picture of 884x1024 and has to be adjusted if a ...
       different resolution is used; the size of the matrix M ...
       above also has to be adjusted if a different ...
       resolution is used
13 M2=M2(1:884,:);
14 %Stores the picture in the Matrix M; if there's more than ...
       one picture the hole procedure between M2= and ...
       M(:,:,k)=M2; has to be done for all of them where k is ...
       index of the picture being loaded in that particular ...
       command sequence
15 M(:,:,1)=M2;
16 %%%%%%%%%%%%%%%%%%%%%%%%%ROI%%%%%%%%%%%%%%%%%%%%%%%%%%%%%%%%%
17 %This allows to select a region of interest for all ...
       pictures by defining its to right (ru) and its bottom ...
       left (ld) corner and putting a 1 at
18 %ROI=0;
19 Roi=0;
20 if Roi==1
21 ru=[254;700];
22 ld=[597;800];
23 ltr=ru(1):ld(1);
24 ttb=ru(2):ld(2);
25 M=M(ttb,ltr,:);
26 end
27
```

74

```
28  %%%%%%%%%%%%%%%%%%%%SNR-calculations%%%%%%%%%%%%%%%%%%%%%%%%
29  %Here some vectors are defined in which all the properties ...
        investigate (SNR,SNR in dB, Signal, Noise(sig)) will ...
        be store in the same order as the indices given when ...
        loading the pictures above
30  SNR_v=zeros(1,numberofpictures);
31  SNRdB_v=zeros(1,numberofpictures);
32  sig_v=zeros(1,numberofpictures);
33  Signal_v=zeros(1,numberofpictures);
34  %This loop calls the function SNRMedian2 which is doing ...
        the actual calculation
35  for k=1:numberofpictures
36      %Variable that allows with slight modifications to the ...
            script to also store the denoise pictures of the ...
            median if wanted
37      Mhelp=double(M(:,:,k));
38      %Calls the function doing the actual SNR calculation ...
            which is descripted later
39      [sig,SNR,SNRdB,Signal] = SNRMedian2(Mhelp);
40      %Stores the results of the calculation in the vectors ...
            defined above
41      Signal_v(k)=Signal;
42      SNR_v(k)=SNR;
43      SNRdB_v(k)=SNRdB;
44      sig_v(k)=sig;
45      %Displays the progress of the overall calculation ...
            since calculation a couple of pictures can take a ...
            minute or two
46      Progress=round(k./numberofpictures.*100);
47      disp(['progress:  ',num2str(Progress), '%'])
48
49  end
50  %Clears the Display from the progress being displayed and ...
        displays the total time needed to calculate all SNRs
51  clc
52  time=toc;
53  disp(['Rechenzeit: ',num2str(time),' sek'])
```

This script is the function SNRMedian2 doing the actual estimation of the
SNR. It requires a picture with the data bar already cut out as input. The
output is the estimated noise, signal, SNR in absolute values and dB, the
denoised picture and the picture consisting only of noise. This script also
requires the medfilt2 function from the image processing toolbox of matlab
to be installed.

```
1  %Defines a function that calculates the SNR from one ...
       picture without data bar
```

75

```matlab
2  function [sig,SNR,SNRdB,Signal,Mfilt,MNoise] = SNRMedian2(M)
3  %M...original picture without data bar
4  %sig...std of the estimated noise
5  %SNR...SNR as Signal/Noise
6  %SNRdB...SNR in decibel
7  %Signal...estimated signal
8  %Mfilt...denoise picture
9  %MNoise...picture consisting of only noise
10 %This line deactivates a warning that the polynomial fit ...
       below is bad conditioned which is irrelevant to the ...
       script but it's still disturbing when it pops up all ...
       the time
11 warning('off','MATLAB:polyfit:RepeatedPointsOrRescale')
12 %Turns the grayscale picture into a matrix of numbers of ...
       class double
13 M=double(M);
14 %Applies the matlab-build-in 2D-median filter to generate ...
       the denoise picture
15 Mfilt=medfilt2(M);
16 %Calculates the picture consisting of only noise
17 MNoise=M-Mfilt;
18 %Gets the height and width of the picture because they are ...
       needed to calculate the signal
19 high=numel(M(:,1));
20 width=numel(M(1,:));
21 %Defines a vector in which the signal estimate of every ...
       line is written
22 Signal_line=zeros(1,high);
23 %Defines a vector in which the points in the middle of the ...
       jump from background to copper wire will be stored
24 Imax_line=zeros(1,high);
25 %This loop estimates the signal for every line in the picture
26 for k=1:high
27 %Defines a vector with the values the kth-line
28 v=M(k,:);
29 %Fits a polynomial into the line of the picture
30 p=polyfit(1:width,v,20);
31 %Derivate the polynomial
32 pd=polyder(p);
33 %Determines the maximum of the derivate of the polynomial, ...
       which is the point in the middle of the jump from ...
       background to copper wire
34 [Wmax,Imax]=max(abs(polyval(pd,50:width-50)));
35 Imax=Imax+49;
36 %Estimates the signal for this line as Absolut value of ...
       the average of every left of the maximum of the ...
       derivation of the polynomial - the average of every ...
       right of that
37 Signal_line(k)=abs(mean(v(1:Imax))-mean(v(Imax:end)));
```

```matlab
38  %Stores the points in the middle of the jump from ...
        background to copper
39  Imax_line(k)=Imax;
40  end
41  %Estimates the signal as average of the estimates of the ...
        signal for every line
42  Signal=mean(Signal_line);
43  %Calculates the average position of the transition form ...
        background to copper wire
44  Imean=mean(Imax);
45  %Estimates the Noise whilst excluding the area around the ...
        transition form background to copper wire
46  Mh=[MNoise(:,1:(Imean—50)),MNoise(:,(Imean+50):end)];
47  sig=std(Mh(:));
48  %Calculates the SNR in absolute values and dB
49  SNR=Signal./sig;
50  SNRdB=10.*log10(SNR);
51  %Switches the warning back on again
52  warning('on','MATLAB:polyfit:RepeatedPointsOrRescale')
53  end
```

8.2 Source code of the linescan script

Figure 97 shows the block diagram of the Labview script designed for the linescan measurements. It is a modification of a buffer read block diagram for the Keithley 6485 provided by Keithley.
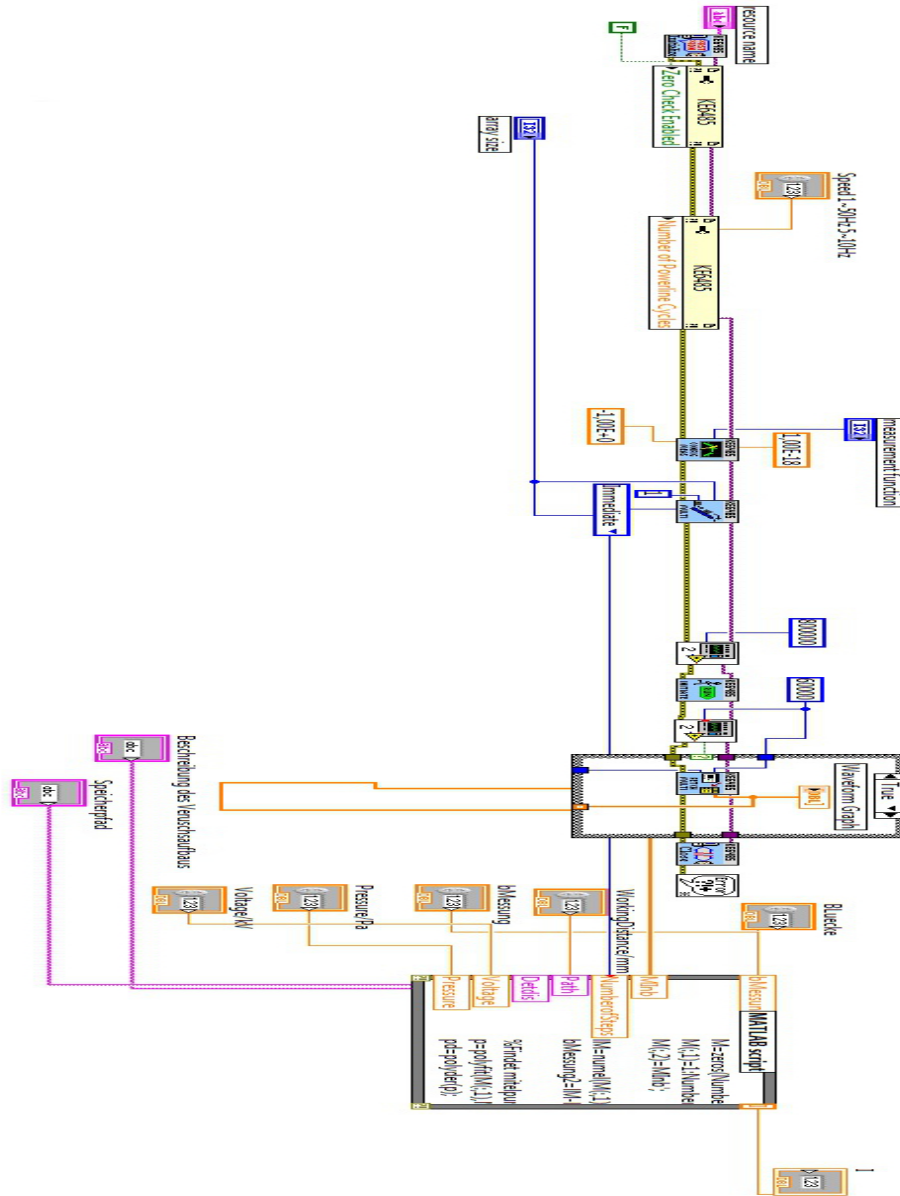
Figure 97: Block diagram of the Labview script designed for the linescan measurements.

Figure 98 shows the user interface of the Labview script designed for the linescan measurements.
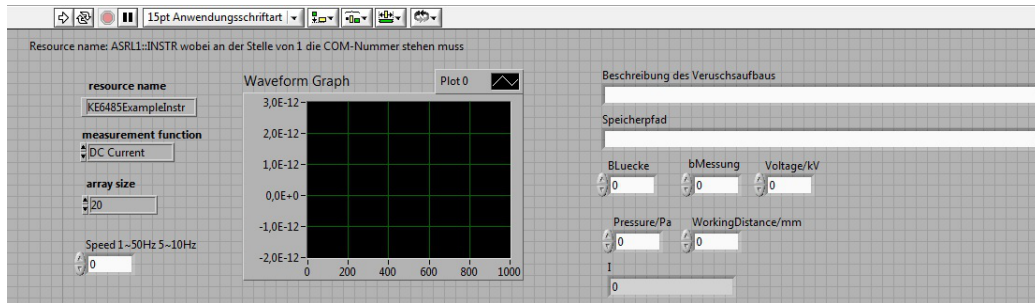
Figure 98: UI of the Labview script designed for the linescan measurements.

This is the matlab script implemented in the labview script above.

```matlab
1  %Defines a vector to store the data from the ...
       measurement(MInb) and enumerate them
2  M=zeros(NumberofSteps,2);
3  M(:,1)=1:NumberofSteps;
4  M(:,2)=MInb';
5
6  %bMessung is a variable that cuts of the data points just ...
       a the end and beginning of the measurement during the ...
       search for the jump in current because they can ...
       interfere with the search
7  lM=numel(M(:,1));
8  bMessung2=lM-bMessung;
9
10 %Finds the point where the current jumps using a ...
       polynomial fit in the same way as the SNR-estimator
11 p=polyfit(M(:,1),M(:,2),20);
12 pd=polyder(p);
13 [Wmax,Imax]=max(polyval(pd,M(25:(lM-25),1)));
14 Imax=Imax+24;
15 Imax=M(Imax,1);
16
17 %Fits the lines onto the results; one in the region ...
       outside the cup; the other in the region inside the cup
18 if and(Imax > bMessung,Imax < bMessung2)
19 punten=polyfit(M((Imax-bMessung):(Imax-bLuecke),1),...
20 M((Imax-bMessung):(Imax-bLuecke),2),1);
21 poben=polyfit(M((Imax+bLuecke):(Imax+bMessung),1),...
22 M((Imax+bLuecke):(Imax+bMessung),2),1);
23 elseif Imax > bMessung
```

```matlab
24  punten=polyfit(M((Imax—bMessung):(Imax—bLuecke),1),...
25  M((Imax—bMessung):(Imax—bLuecke),2),1);
26  poben=polyfit(M((Imax+bLuecke):lM,1),M((Imax+bLuecke):lM,2),1);
27  elseif Imax < bMessung2
28  punten=polyfit(M(1:(Imax—bLuecke),1),M(1:(Imax—bLuecke),2),1);
29  poben=polyfit(M((Imax+bLuecke):(Imax+bMessung),1),...
30  M((Imax+bLuecke):(Imax+bMessung),2),1);
31  else
32  punten=polyfit(M(1:(Imax—bLuecke),1),M(1:(Imax—bLuecke),2),1);
33  poben=polyfit(M((Imax+bLuecke):lM,1),M((Imax+bLuecke):lM,2),1);
34  end
35
36  %Calculates the current as line fit inside the cup minus ...
        line fit outside the cup at the point where the ...
        current jumps because the beam crosses the edge
37  M3=[polyval(poben,M(Imax,1)),polyval(punten,M(Imax,1))];
38  I=M3(1)—M3(2);
39  %Generates a figure showing the results and the plot in ...
        order to allow the experimenter to check wheatear the ...
        fits have been done accurately or not immediately
40  figur=figure
41  plot(M(:,1),M(:,2),M(:,1),polyval(p,M(:,1)),Imax,M(Imax,2),...
42  '*',M(:,1),polyval(punten,M(:,1)),M(:,1),...
43  polyval(poben,M(:,1)),[M(Imax,1),M(Imax,1)],M3)
44  grid on
45  xlabel('distance/a.u.')
46  ylabel('I/nA')
47  title(['Aufbau: ',Detdis,' Pressure: ',num2str(Pressure), ...
        ' Pa ', 'Voltage: ',num2str(Voltage), ' kV ', ' WD: ', ...
        num2str(WD), ' mm ', 'Beamcurrent: ', num2str(I), ' nA'])
48  save([Path,'\',Detdis,num2str(Voltage),'kV', ...
49  num2str(Pressure),'Pa',num2str(WD),'mm','.txt'],'M','—ascii')
50  saveas(figur,[Path,'\',Detdis,num2str(Voltage),'kV',...
51  num2str(Pressure),'Pa',num2str(WD),'mm'],'fig')
```

8.3 Example pictures with different SNR

These are some examples of pictures of the copper wire at different SNRs taken with the Q200.
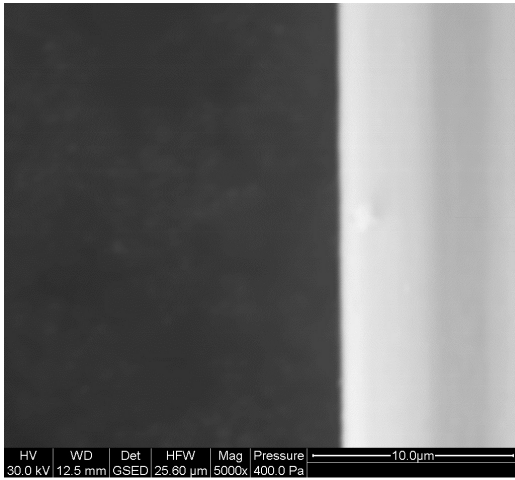

Figure 99: Copper wire on C-tape at SNR = 22.
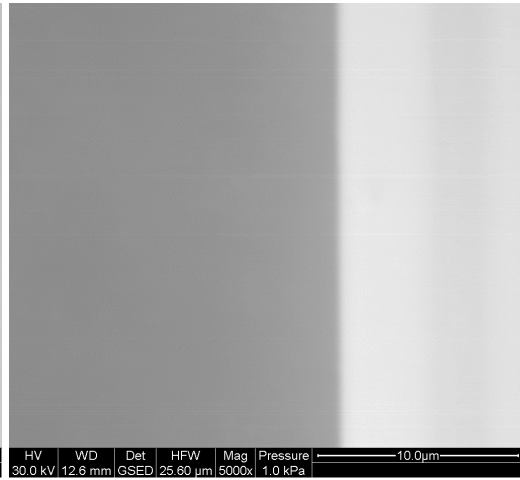
Figure 100: Copper wire on C-tape at SNR = 18.5.
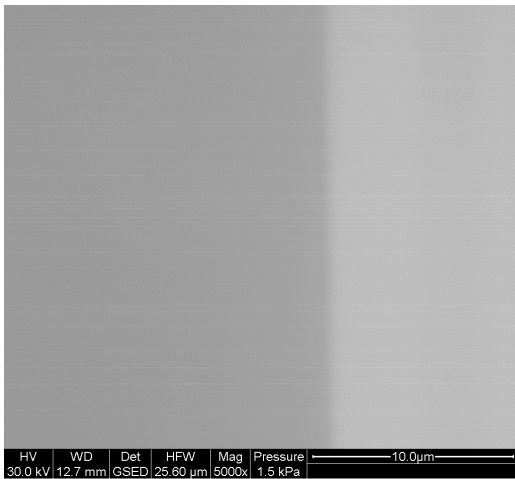

Figure 101: Copper wire on C-tape at SNR = 13.5.
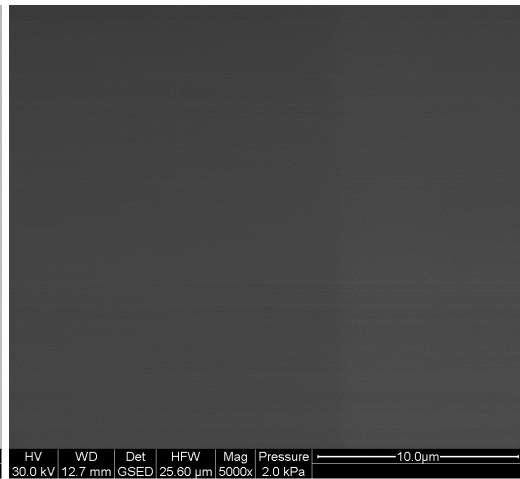
Figure 102: Copper wire on C-tape at SNR = 3.5.

8.4   Pictures of the original and new bullet

Figure 103: Original bullet viewed from the side.

Figure 104: New bullet viewed from the side.

Figure 105: Original bullet viewed from the top.

Figure 106: New bullet viewed from the top.

## 8.5 Pictures of the electrode shapes used in chapter 5.2.2
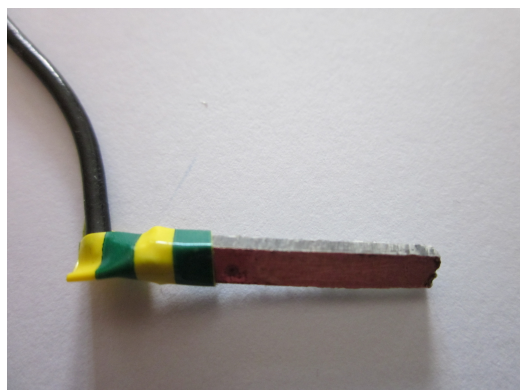
Figure 107: Flat electrode.


Figure 108: Blade electrode.
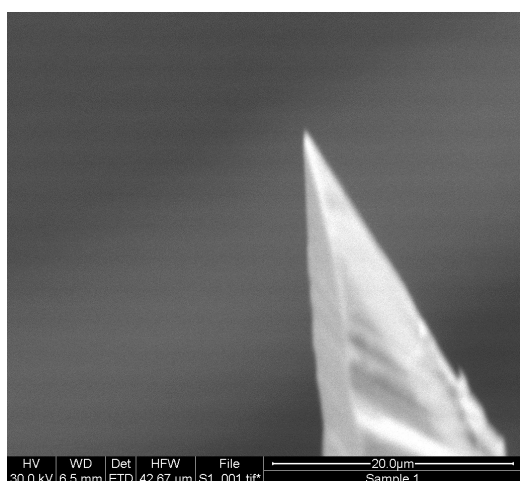
Figure 109: Tip of the 0.5 µm tip electrode.
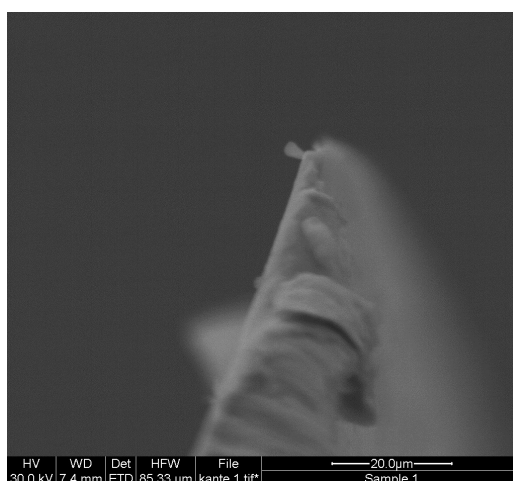
Figure 110: Edge of the blade electrode.

## 8.6 Full results of the tip size measurements in chapter 5.2.2
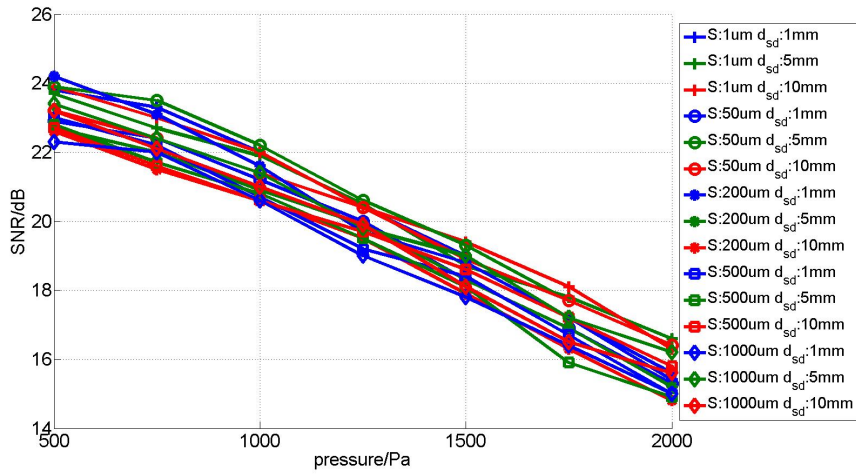
Figure 111: Full results: SNR as a function of pressure for different tip sizes(S) and sample-detector distances(d_{sd}) using water vapor as imaging gas.
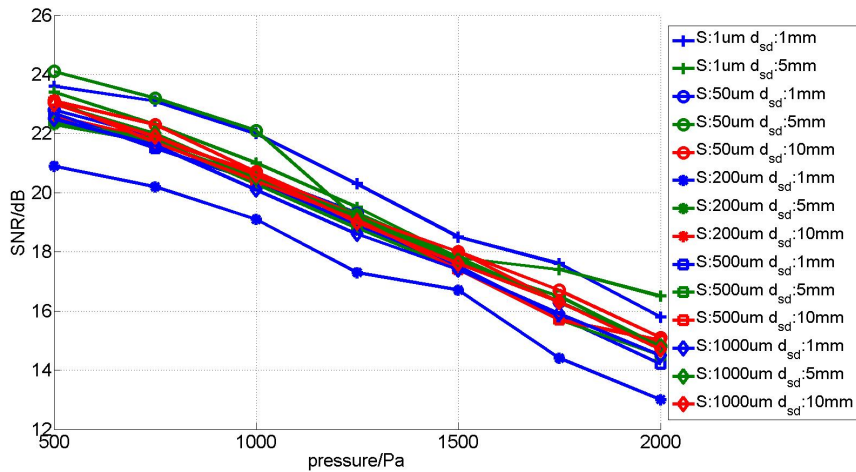

Figure 112: Full results: SNR as a function of pressure for different tip sizes(S) and sample-detector distances(d_{sd}) using air as imaging gas.

8.7 Environmental distances used in figure 81, 85

Table 1: Environmental distances used in figure 81, 85

p...chamber pressure
ED_{GSED}...Environmental distance using the GSED
ED_{ESED}...Environmental distance using the ESED
ED_{SSD}...Environmental distance using the SSD

p/Pa	ED_{GSED}/mm	ED_{ESED}/mm	ED_{SSD}/mm
H_2O:			
200	2.5	1.2	1.2
400	2.5	1.2	1.2
600	1.7	1.2	1.2
800	1.0	1.2	1.2
1000	0.5	1.2	1.2
1200	0.2	1.2	1.2
1400	0.1	1.2	1.2
1600	0.1	1.2	1.2
1800	0.1	1.2	1.2
2000	0.1	1.2	1.2
2200	0.1	1.2	1.2
2400	0.1	1.2	1.2
Ambient air:			
200	2.5	1.2	1.2
400	2.5	1.2	1.2
600	0.6	1.2	1.2
800	0.1	1.2	1.2
1000	0.1	1.2	1.2
1200	0.9	1.2	1.2
1400	0.9	1.2	1.2
1600	1.0	1.2	1.2
1800	0.5	1.2	1.2
2000		1.2	1.2
2200		1.2	1.2
2400		1.2	1.2
2600		1.2	1.2
2700		1.2	1.2